SAND2021-7616J

MATERIAL INTERACTIONS IN SEVERE ACCIDENTS - BENCHMARKING THE MELCOR V2.2 EUTECTICS MODEL FOR A BWR-3 MARK-I STATION BLACKOUT: PART I - SINGLE CASE ANALYSIS

Lucas I. Albright[a,b,*], Nathan Andrews[a], Larry L. Humphries[a], Markus H.A. Piro[c], Glenn E. Sjoden[b], David L. Luxat[a], Tatjana Jevremovic[d]

[a]*Sandia National Laboratories,1515 Eubank, Albuquerque, New Mexico 87123, United States of America*
[b]*University of Utah, 201 Presidents Cir, Salt Lake City, Utah 84112, United States of America*
[c]*Ontario Tech University, 2000 Simcoe Street North, Oshawa, Ontario L1G OC5, Canada*
[d]*International Atomic Energy Agency, Wagramer Str.5, 1220 Vienna, Austria*

ABSTRACT

In this analysis, the two material interaction models available in the MELCOR code are benchmarked for a severe accident at a BWR under representative Fukushima Daiichi boundary conditions. This part of the benchmark investigates the impact of each material interaction model on accident progression through a detailed single case analysis. It is found that the eutectics model simulation exhibits more rapid accident progression for the duration of the accident. The slower accident progression exhibited by the interactive materials model simulation, however, allows for a greater degree of core material oxidation and hydrogen generation to occur, as well as elevated core temperatures during the ex-vessel accident phase. The eutectics model simulation exhibits more significant degradation of core components during the late in-vessel accident phase – more debris forms and relocates to the lower plenum before lower head failure. The larger debris bed observed in the eutectics model simulation also reaches higher temperatures, presenting a more significant thermal challenge to the lower head until its failure. At the end of the simulated accident scenario, however, core damage is comparable between both simulations due to significant core degradation that occurs during the ex-vessel phase in the interactive materials model simulation. A key difference between the two models' performance is the maximum temperatures that can be reached in the core and therefore the maximum ΔT between any two components. When implementing the interactive materials model, users have the option to modify the liquefaction temperature of the ZrO_2-interactive and UO_2-interactive materials as a way to mimic early fuel rod failure due to material interactions. Through modification of the liquefaction of high melting point materials with significant mass, users may inadvertently limit maximum core temperatures for fuel, cladding, and debris components.

HIGHLIGHTS

- The eutectics model simulation exhibits accelerated accident progression in comparison to the interactive materials model simulation

* Corresponding Author
Email Addresses: lialbri@sandia.gov, (Lucas I. Albright), nandrew@sandia.gov (Nathan Andrews), llhumph@sandia.gov (Larry L. Humphries), dlluxat@sandia.gov (David L. Luxat), T.Jevremovic@iaea.org (Tatjana Jevremovic)

- Earlier degradation of fuel components is observed for the eutectics model simulation
- The eutectics model simulation exhibits greater quantities of both molten and refrozen, conglomerate debris
- Greater masses of debris are formed and ejected from the RPV in the eutectics model simulation
- The interactive materials model simulation exhibits lower peak temperatures for fuel, cladding, and debris components

Keywords: MELCOR, Severe Accident, Material Interactions, Eutectics Model, Interactive Materials Model

1. INTRODUCTION

The treatment of material interactions in modern severe accident analyses is evolving. For over two decades, material interactions have been known to accelerate the degradation of reactor core systems, structures, and components (SSCs) during severe accidents in light water reactors (LWRs) [1]. Recently, severe accident experts have recognized the need to improve traditionally implemented material interaction models. Previously, modification of global, constituent material melting points of known reactions was sufficient to capture material interaction physics to the necessary degree accuracy in the MELCOR code [2] [3]. Today, the MELCOR code is moving towards higher fidelity material interaction models thanks to insights gained by post-accident analysis of the severe accidents at Fukushima Daiichi and expectant safety analysis of emerging reactor technologies. With the advent of mature accident tolerant fuels and next-generation reactor designs, it is imperative that accurate treatment of material interactions be incorporated into severe accident codes to fully capture the complex behavior of material interactions and multi-component mixtures under severe accident conditions.

Design-specific SSCs as well as materials will determine the importance of material interactions to core damage progression. As a matter of fact, interactions between SSC materials are known to occur at all temperatures. At low temperatures, however, the reaction rate is often slow enough that the effect is negligible. At higher temperatures, the reaction rate accelerates. Under prolonged extreme temperature conditions, as experienced during a severe accident, material interactions can contribute to, or even cause, early failure of core SSCs (e.g. control rods, fuel assemblies, and other core support structures) and fission product barriers (FPBs) (e.g. fuel matrix, fuel cladding, reactor pressure vessel (RPV)) [4] [5]. Such interactions can be solid-solid interactions that form low melting point alloys and eutectic mixtures, or chemical dissolution of solids by a liquid mixture. After failure of SSCs and FPBs, core materials relocate downward and coolable rod-like geometry may be lost – coolable geometry is impaired by phenomena that obstruct the open area of flow channels including bowing, ballooning, candling, and collapse. Of prime importance are material interactions that can lead to early relocation of reactor fuel and fission products (FPs), commonly referred to as “heat-bearing materials” because of their associated decay heat. For LWRs, the interaction between UO_2 fuel and Zr-based fuel cladding materials are known to cause early relocation of heat-bearing materials [1].

Material changes to the fuel-clad system begins with autocatalytic Zr oxidation[1] and the formation of an external oxide scale. Cladding oxidation produces oxygen stabilized α-Zr(O) until the point of oxygen saturation, after which, an oxide scale (ZrO_2) begins to form [1]. The ZrO_2 scale continues to grow as oxygen from the steam diffuses through the scale to oxygen-stabilized and unoxidized portions of the cladding. Internally, oxidation of Zr-based cladding also occurs by oxygen diffusing from the UO_2 fuel pellet at high temperatures. Similarly to external oxidation of Zr-based cladding, the uptake of oxygen by Zr-based cladding from the UO_2 results in α-Zr(O) and hypo-stoichiometric UO_{2-x} that eventually becomes a UO_2 + U (uranium oxide plus liberated metallic uranium) layer [6]. The U metal within this layer will interact with Zr in the neighboring α-Zr(O) layer forming a (U,Zr) alloy. The (U,Zr) alloy in the α-Zr(O) penetrates the full depth of the layer, linking a (U,Zr) layer low in oxygen to the UO_2 + U layer. Finally, there is a second layer of α-Zr(O) before the unoxidized Zr layer. At temperatures above the melting point of zirconium-based cladding, unoxidized portions will melt and dissolve the fuel and oxide scale. The progression of material changes to the fuel clad system are shown in Figure 1.

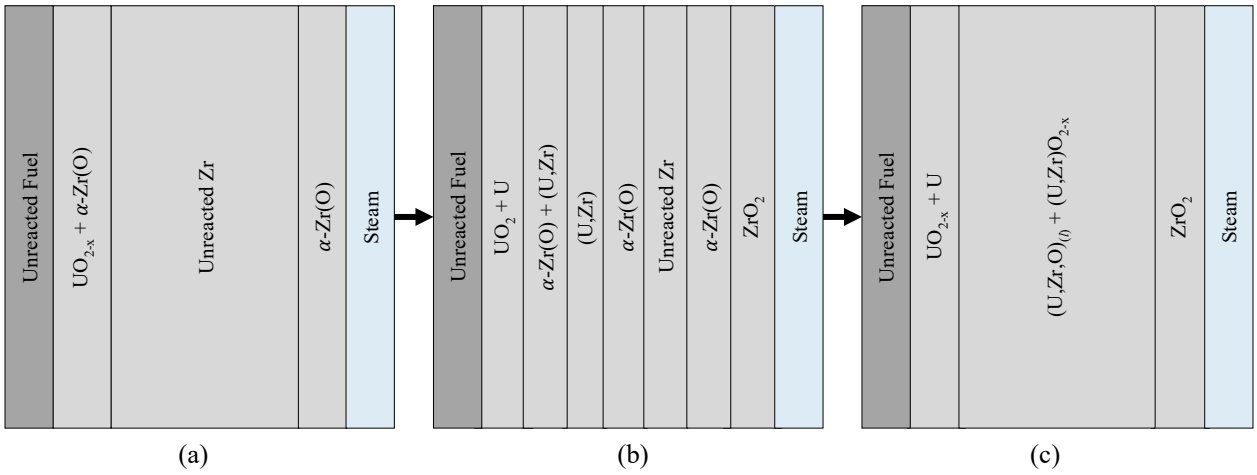

Figure 1. Fuel-clad system material evolution. (a) relatively unreacted fuel-clad, (b) significantly reacted fuel-clad, (c) significantly reacted fuel-clad with α-Zr(O) melting point < T < ZrO_2 melting point.[2]

Dissolution of UO_2 and ZrO_2 by Zr-based cladding occurs rapidly after the onset of melting (around 2000 K-2100 K), far below melting points of either UO_2 (approximately 3100 K) and ZrO_2 (about 3000 K) [1]. Furthermore, UO_2 dissolution by molten Zr-based cladding occurs more quickly than ZrO_2 dissolution. The resulting molten material is a U-Zr-O mixture that continues to dissolve both UO_2 and ZrO_2, accumulating fission products and degrading the protective oxide (ZrO_2) scale until the melt refreezes, or the oxide scale fails. After failure of the oxide scale, the U-Zr-O melt and any fission products contained within it will relocate downward

[1] It should be noted that oxidation of core materials, and Zr in particular, is a significant source of combustible hydrogen gas. Accumulation of hydrogen gas produced by core material oxidation is safety significant as deflagration and/or detonation may occur.

[2] MELCOR does not model fuel rod degradation at the level of detail shown in Figure 1 (e.g. layering in the cladding).

in the core region by the candling process, redistributing the heat production in the core and leading to greater thermo-chemical challenges to FPBs and SSCs at lower core elevations.

The chemical dissolution of both UO_2 and ZrO_2 by Zr-based cladding is driven by two primary mechanisms: oxygen diffusion and natural-convection mass transfer [7] [8]. Natural-convection mass transfer occurs when dissolved materials create local density gradients that lead to mixture circulation – standard material densities are as follows: liquid U ~17 g/cm^3, Zr-based cladding ~6 g/cm^3, ZrO_2 ~5.68 g/cm^3 [6]. Density differences caused by UO_2 dissolution are much larger than those caused by ZrO_2 dissolution. Consequently, natural-convection mass transfer has a greater influence on UO_2 dissolution. The convective mass transfer process is defined as [9] [10]:

$$\mathrm{UO_{2-x}} + \mathrm{Zr(O)}_{(l)} \rightarrow \mathrm{(U, Zr, O)}_{(l)} \tag{1}$$

$$\mathrm{ZrO_2} + \mathrm{Zr}_{(l)} \rightarrow 2\mathrm{Zr(O)}_{(l)} \tag{2}$$

Oxygen diffusion-controlled dissolution follow the chemical path as follows:

$$\mathrm{UO_2} + \mathrm{Zr}_{(l)} \rightarrow \mathrm{UO_{2-x}} + \mathrm{Zr(O)}_{(l)} \rightarrow \mathrm{(U, Zr, O)}_{(l)} \tag{3}$$

$$\mathrm{ZrO_2} + \mathrm{Zr}_{(l)} \rightarrow \mathrm{ZrO_{2-x}} + \mathrm{Zr(O)}_{(l)} \tag{4}$$

In the case of UO_2 dissolution, the process occurs in two stages: an initial period of rapid convection-based dissolution that terminates when the resulting mixture reaches U and O saturation and a subsequent period of diffusion-based dissolution and precipitation within the melt; oxygen diffusion from the remaining solid fuel into the melt causes oversaturation of the liquid and precipitation of $(U,Zr)O_{2-x}$ [11]. Oxygen diffusion-based dissolution drives ZrO_2 dissolution because molten Zr-based cladding and ZrO_2 have similar densities (i.e. density differences are too small for appreciable natural convection to occur) [9]. Both UO_2 and ZrO_2 dissolution are heavily influenced by the oxygen content within the melt and any external oxygen sources (e.g. steam). Oxygen diffusion-controlled dissolution of a component can only occur above the melting point of Zr-based cladding after surface wetting of the component by the melt. Surface wettability is material dependent, and different for the various material combinations in the fuel-clad-oxide scale complex [12].

At the fuel-clad interface, oxygen diffuses from the UO_2 into the liquid Zr-based cladding, forming hypo-stoichiometric UO_{2-x} and α-Zr(O). In time, the hypo-stoichiometric UO_{2-x} becomes uranium metal and dissolves into the α-Zr(O), forming a U-Zr-O melt. A similar process occurs externally as oxygen diffuses from the oxide scale to the forming hypo-stoichiometric ZrO_{2-x} and α-Zr(O) [9] [10]. As with cladding oxidation and the formation of the oxide scale, the oxygen diffusion-controlled dissolution process is governed by parabolic kinetics. Parabolic kinetics generally apply to processes where the diffusion is rate-limited by the formation of a protective oxide scale [13]. Mathematically, such a process can be represented by the parabolic rate law, which for reaction processes that include an initial transient period of accelerated reaction kinetics before reaching steady-state parabolic kinetics, takes the following form:

$$(x(T,t) - x_o)^2 = K(T)t \tag{5}$$

where $x(T,t)$ is the mass or weight percent of dissolved material [kg or wt.%] at a given temperature T [K] and time t [s], x_o is the mass or weight percent of that material [kg or wt.%] dissolved during the initial period of rapid dissolution, and $K(T)$ is a temperature dependent rate constant $\left[\frac{\text{wt.\%}^2}{\text{s}}\right]$. For many reaction processes, the rate constant is given by the Arrhenius relation shown by:

$$K(T) = A\exp\left(\frac{-B}{RT}\right) \tag{6}$$

with experimentally derived correlation constants A and B have units $\left[\frac{\text{wt.\%}^2}{\text{s}}\right]$ and $\left[\frac{\text{J}}{\text{mol}}\right]$, respectively, and the universal gas constant R has units of $\frac{\text{J}}{\text{K·mol}}$. Experimentally derived constants for the correlation were derived by Hoffman et al. and can be found in reference [14].

There are many material interactions that can occur in LWRs that affect core damage progression. Other notable material interactions identified in early studies include Fe/Zr, Zr/Ni, and Fe/B, which impact the integrity of a number of core structures including control rods, grid spacers, and fuel canisters. The earliest interactions to occur in LWRs start near 1200 K (Fe/Zr and Zr/Ni reactions) followed by Fe/B reactions near 1450 K [1]. Historically, research efforts have been dedicated to understanding the pseudo-binary systems of constituent materials (e.g. UO_2-ZrO_2 shown in Figure 2). More recent thermodynamic studies have investigated larger material systems and shown that binary systems of constituent materials do not reflect the compounding effects of multi-component systems, including the complex topology of their phase diagrams; prominent multi-component mixtures that relate to LWR technologies are U-Zr-O, U-Zr-O-Fe, and Fe-Zr-B.

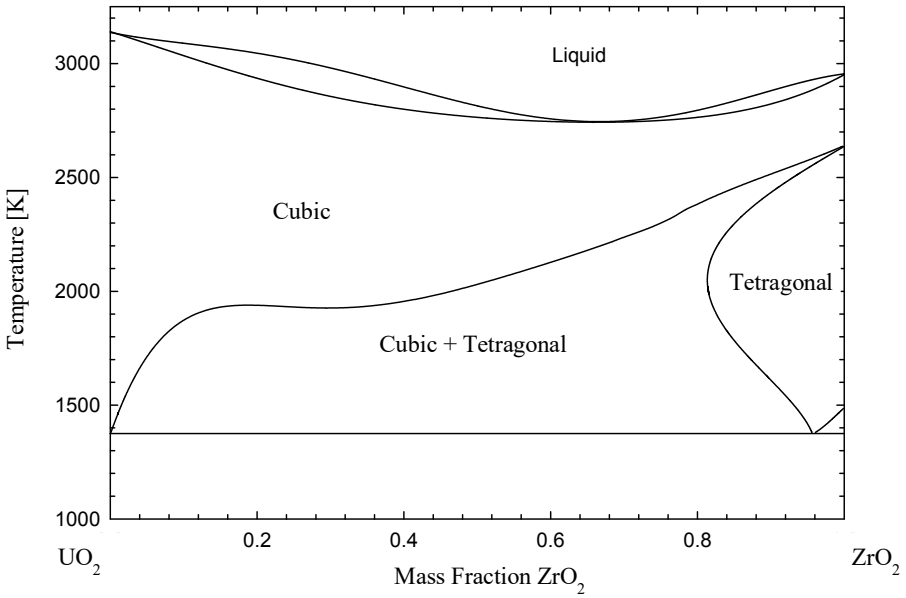

Figure 2. Pseudo-binary phase diagram of the UO_2-ZrO_2 system [15]

In this analysis, the authors have performed a single case, best-estimate analysis using the two material interaction models presently available to MELCOR users for a station blackout (SBO) of a boiling water reactor (BWR) using representative Fukushima Daiichi Unit 1 boundary conditions. The goal of this work is not to replicate the accident progression at Fukushima Daiichi Unit 1, but to perform a fundamental comparison between the eutectics and interactive material models. The single case, best-estimate analysis is performed using MELCOR's eutectics model and repeated using the "interactive materials" model to provide comparison. The eutectics model was recently implemented as the new default treatment for material interactions in MELCOR, replacing the traditionally utilized interactive materials model. Chapter 2 of this analysis details the authors' approach and includes a summary of MELCOR V2.2 capabilities and relevant models, a description of the plant model used in the analysis, and the analysis comparison methodology. In chapter 3, the authors present analysis results and discuss their importance, while chapter 4 concludes the analysis and highlights key findings.

2. MATERIALS AND METHODS

2.1. MELCOR V2.2

MELCOR is a fully integrated, engineering-level severe accident code developed at Sandia National Laboratories for the U.S. Nuclear Regulatory Commission (USNRC) to support plant licensing and regulatory efforts [2] [3]. MELCOR's capabilities encompass the breadth of severe accident phenomena, spanning the initiating event through the release of radioactive materials to the environment for multiple reactor types. MELCOR uses the control volume approach to capture plant response to accident conditions and grants users significant flexibility when defining plant parameters, from plant nodalization, to correlation and built-in model parameter modification through control functions and sensitivity coefficients. While previous versions of MELCOR were predominately parametric, phenomenological models in the current version are mostly mechanistic; parametric models in general, are limited to phenomena with large uncertainties. This analysis is performed with MELCOR V2.2 revision 15348 [2] [3].

Renewed interest in the importance of material interactions has brought a change in the default treatment of material interactions in MELCOR. The following built-in MELCOR material classes are relevant to this analysis: ZR (representative of Zr-based alloys), ZRO2 (representative of ZrO_2), UO2 (representative of UO_2-based nuclear fuel), SS (representative of stainless steel), SSOX (representative of oxidized stainless steel), INC (representative of inconel), B4C (representative of B_4C control material). In the present section, MELCOR material designations are used in order to maintain consistency with other MELCOR reference materials.

2.1.1. MELCOR Eutectics Model

The eutectics model is currently implemented as the default treatment for material interactions in the MELCOR code but can be overwritten by definition of the necessary interactive materials model parameters. MELCOR's eutectics model enables explicit treatment of material interactions and has three main components: reactions that can cause early failure of fuel and control rods, composition-dependent mixture properties (e.g. reduced liquefaction temperatures), and the dissolution of intact components by molten mixtures.

Molten mixture properties resulting from material interactions are treated for mixtures that have been converted to conglomerate debris. Conglomerate debris materials are associated with core components [3]and treated as coherent mixtures. Material pairs corresponding to material interactions treated by MELCOR become part of the conglomerate debris mixture by one of three processes: (1) intact solid components reach their melting point, (2) two intact solid components in mechanical contact reach their eutectic temperature, or (3) dissolution of intact solid components by a liquid mixture.

Eutectic Reactions
MELCOR models two eutectic reactions that can lead to early failure of SSCs in BWRs: the eutectic interaction between zirconium-based fuel cladding and inconel grid spacers (ZR/INC); and the eutectic interaction between B4C and steel control rod cladding (SS/B4C). The ZR/INC reaction occurs at 1400 K by default and can cause early failure of fuel rods, while the SS/B4C occurs at 1520 K by default and can lead to early failure of the BWR control blades. Default reaction temperatures are defined to approximate the point when the reaction rate of material interactions between two contacting solids causes significant liquefaction. Molten material formed by these eutectic reactions becomes conglomerate debris associated with that component.

Composition-Dependent Mixture Properties
The simplified eutectics model has built-in capability to treat six pseudo-binary mixtures as surrogates for the complex, multi-component systems that may develop locally during severe accidents, shown in Table 1. The molar ratios and "eutectic temperature" of each material pair are derived from binary phase diagrams for each mixture.

Table 1. MELCOR Eutectics Model Binary Material Interaction Parameters

Material Pairs		Molar Ratio	Eutectic Temperature [K]
ZR	INC	0.76/0.24	1210
ZR	SS	0.76/0.24	1210
ZRO2	UO2	0.50/0.50	2450
ZR	B4C	0.43/0.57	1900
SS	B4C	0.69/0.31	1420
ZR	Silver-Indium-Cadmium (AGINC)	0.67/0.33	1470

When the eutectics model is active, the solidus temperature of a mixture is calculated as the mole-weighted combination of the solidus temperatures of every binary combination of material pairs in the mixture:

$$TS_{mix} = \frac{\sum_j \sum_{i \neq j} f_i f_j TS_{ij}}{\sum_j \sum_{i \neq j} f_i f_j} \quad (7)$$

where f_i is the mole-fraction of the first constituent material, f_j is the mole-fraction of the second constituent material, and TS_{ij} is the solidus temperature for a mixture of materials *i* and *j* with

[3] Core components are MELCOR modeling objects for the different types of structures and debris found in a reactor core (e.g. fuel, supporting structure, particulate debris, etc.)

the same relative proportions as the total mixture. Currently, TS_{ij} is obtained from either mole-weighting of each constituent material solidus temperature or one of six pseudo-binary phase diagrams shown in Table 1. For the material pairs in Table 1, the solidus temperature of a mixture is treated as mole-weighted average of the eutectic temperature and solidus temperature of the constituent in excess of the eutectic composition:

$$T_{solidus}^{mix} = f_{eutectic}\, T_{eutectic} + f_{excess}\, T_{solidus}^{excess} \quad (8)$$

where $T_{solidus}^{mix}$ is the solidus temperature of the mixture, $f_{eutectic}$ is the mole-fraction of the primary constituent, $T_{eutectic}$ is the eutectic temperature of the mixture, f_{excess} is the mole-fraction of the constituent in excess ,and $T_{solidus}^{excess}$ is the solidus temperature of the constituent in excess

MELCOR does not perform Gibbs free energy minimization to evaluate the phase of material mixtures. The liquidus temperature of each component and the eutectic mixture are set to the solidus temperature plus 0.01 K. The specific enthalpy of the eutectic mixture is determined according to mixture temperature and phase. For mixture temperatures below the calculated solidus, weighted individual enthalpies are added together; extrapolated solid enthalpies are used for any constituent that would normally be liquid. At mixture temperatures greater than the calculated mixture liquidus, mass weighted individual enthalpies are added together; extrapolated liquid enthalpies are used for any constituent that would normally be solid. When mixture temperatures lie between the solidus and liquidus of a mixture, linear interpolation between the solidus and liquidus enthalpy is used. The latent heat of fusion for a eutectic mixture is taken as the difference between the liquid and solid enthalpy as determined by the mass weighted enthalpies. All other properties of formed mixtures are defined as the mass-weighted averages of constituent properties.

Chemical Dissolution of Solids

MELCOR has a built-in capability to treat the chemical dissolution of solids. The rate of dissolution is governed by parabolic kinetics using experimentally obtained rate constants. Currently, MELCOR only allows material mixtures to dissolve UO2 and ZRO2. UO2 and ZRO2 dissolution occurs only if the enthalpy of a molten mixture exceeds its liquidus enthalpy. Two limitations are employed by MELCOR on the chemical dissolution of UO2 and ZRO2: mixture enthalpy limits and parabolic rate limitations. The amount of dissolved material is first predicted by the parabolic rate reported by Hofmann, et al., 1989 [14]. This predicted mass is then used to calculate mixture enthalpy to ensure conservation of energy. If the updated mixture enthalpy is too high, then the mass will be reduced until the updated mixture enthalpy is equal to the liquidus enthalpy of the updated mixture composition. Thus, the parabolic rate is treated as an upper bound for dissolution and is used for all mixtures, including mixtures with a low ZR content for which the predictions become more inaccurate. The parabolic rate limitation for UO2 and ZRO2 dissolution in MELCOR is implemented as[4]:

$$\left(x_j^f\right)^2 = \left(x_j^i\right)^2 + K_j\, \Delta t \quad (9)$$

[4] Eq. 9 is a discretized form of the time and temperature dependent parabolic rate equation shown in Eq. 5.

where x_j^f is the mass fraction of material j at end of time step, x_j^i is the mass fraction of material j at start of time step, Δt is the timestep size, and K_j is the temperature dependent rate constant defined by the Arrhenius equation[5]:

$$K_j = A_j \exp\left(\frac{B_j}{T}\right) \tag{10}$$

MELCOR calculates K_j using the experimental correlations reported by Hofmann et al. [14] for all mixtures, regardless of composition. Application of the dissolution constants obtained experimentally by Hoffman et al., shown in Table 2, introduces error into the predicted dissolution rates as the Zr content decreases in the mixture. Furthermore, the dissolution models for UO_2 and ZrO_2 do not become active until after cladding failure.

Table 2. Parabolic Rate Constants by Material [2] [3]

Solid	$\boldsymbol{A_j}\left[\frac{\text{wt.}\%^2}{\text{s}}\right]$	$\boldsymbol{B_j}$ [K]
ZrO_2	1.47×10^{14}	8.01×10^4
UO_2	1.02×10^{15}	8.14×10^4

2.1.2. MELCOR Interactive Materials Model

Until recently, the interactive materials model was used to capture the effects of material interactions by the MELCOR code. The interactive materials model captured the reduced melting points of core materials caused by material interactions by artificially lowering respective material liquefaction temperatures.

Interactive Materials
The material classes: ZRO2-INT, UO2-INT, and B4C-INT, with identical characteristics to the pure ZRO2, UO2, and B4C material classes, respectively, are available to users with the added option to modify liquefaction temperatures thereby approximating the effect of materials interactions on material phase changes during core degradation. Other material properties available to user-modification as part of the interactive materials model include thermal conductivity, density, and latent heat of fusion. Modifications to the ZRO2-INT, UO2-INT, and B4C-INT material classes are global and are not composition dependent – intact UO2-INT, ZRO2-INT, and B4C-INT materials melt at their reduced liquefaction temperatures without consideration of the availability of other interacting materials or liquids.

Secondary Material Transport
When the interactive materials model is activated, the secondary material transport model is also enabled. This model allows the transport of unmolten secondary materials by candling molten materials to simulate both the dissolution of UO2 by molten ZR and the oxide shell debris that is

[5] MELCOR accounts for the universal gas constant, R, from Eq. 6 in the values reported for B_j shown in Table 2.

carried with candling materials. Two mechanisms of transport are possible using the secondary material transport model. The first option transports a mass of unmolten material defined as a fraction of the candling molten mass:

$$\Delta M_s = F_1 \, \Delta M_m \tag{11}$$

the second option transports an amount of unmolten material equal to a fractional proportion of its existing fraction within a component:

$$\Delta M_s = F_2 \frac{M_{s,total}}{M_{m,total}} \, \Delta M_m \tag{12}$$

where F_1 is the input fraction of the candling molten mass, F_2 is the fraction of proportional relocation, M_s is the unmolten secondary material, M_m is the candling molten mass refrozen (deposited) on a component, $M_{s,total}$ is the total unmolten secondary material mass in the component in the cell of origin, and $M_{m,total}$ is the total material mass in the cell of origin. The secondary material transport model is inactive if the eutectics model is activated.

2.2. Plant Representation

The foundation of the plant model featured in this analysis is the Peach Bottom Nuclear Power Plant (1180 MW(e) BWR/4 reactor, Mk-I containment) model maintained by Sandia National Laboratories (SNL) for the USNRC, which was used in the State of the Art Reactor Consequence Analysis (SOARCA) Peach Bottom Analysis project [16] [17]. Post-Fukushima, a version of the Peach Bottom Nuclear Power plant model was modified by SNL to incorporate accurate design characteristics of the Fukushima Daiichi Unit 1 nuclear reactor (1380 MW(th) BWR/3 reactor, Mk-I containment) – plant characteristics from the model are shown in Table 3 – and used in the Organisation for Economic Cooperation and Development Nuclear Energy Agency (OECD/NEA) Benchmark Study of the Accident at the Fukushima Daiichi Nuclear Power Plant (BSAF) project [18]. In this analysis, boundary conditions representative of the Fukushima Daiichi Unit 1 accident (1F1) that were used during the BSAF project have been preserved and are outlined below. The primary purpose of this analysis is not to reconstruct the severe accident at Fukushima Daiichi Unit 1, but to compare the effect of material interaction models available to MELCOR users on the progression of core degradation and overall plant states. To that end, changes have been made to the plant model that do not necessarily reflect the 1F1.

Table 3. BWR/3 Reactor Model Parameters

Plant Parameter	Value
Rated Core Power [MW_{th}]	1380
Total RPV water inventory [kg]	147634
Number of fuel assemblies [#]	400
Number of control blades [#]	97
Total mass of UO_2 [kg]	77403
Total mass of zircaloy [kg]	30431

Total mass of stainless steel [kg]	47767
Total mass of B_4C [kg]	540
Mass of active region zircaloy cladding [kg]	16779
Mass of upper core, non-active region zircaloy cladding [kg]	2202
Mass of lower core, non-active region zircaloy cladding [kg]	0
Mass of zircaloy in fuel canister [kg]	11451
Mass of stainless steel in control blades [kg]	9000
Mass of stainless steel in top guide tube and upper tie plate [kg]	4420
Mass of stainless steel in core support plate and other stainless steel support structures [kg]	8880
Mass of lower plenum stainless steel support structures [kg]	25467

The nodalization scheme of the plant remains unchanged from the BSAF project [18]. Thermal hydraulic phenomena are modeled in 26 separate control volumes representing the lower plenum and core region, while core degradation phenomena are captured in 88 core cells. The Mark I containment building is discretized into six control volumes and the drywell floor is divided into three regions where debris can accumulate and interact with the concrete floor during molten core concrete interaction (MCCI). The reactor building is discretized into 14 control volumes. More information on the plant nodalization scheme can be found in references [19] (RPV nodalization) and [20] (containment nodalization).

2.2.1. Plant Model Parameters

For the present analysis, the number of safety relief valves (SRVs) operating during the accident sequence has been increased from one to four to accurately represent SRV behavior. Changing the number of safety relief valves operating during the simulation alters the behavior of energy transfer from the primary system to containment including distributing energy rejected from the primary system across four main steam lines (dependent on predicted SRV behavior). Each SRV operates based on its separate pressure setpoints that, in turn, depend on the availability of power. Core degradation forcing functions (e.g. core ring failures, lower head failure, etc.) were used by analysts during BSAF to simulate a forensic reconstruction of key accident signatures observed during 1F1. Such forcing functions have been removed from the plant model, to allow core degradation to proceed according to built-in MELCOR models. By using built-in MELCOR models, a more complete comparison can be made between the eutectic and interactive materials models' effects on core damage progression as predicted by MELCOR. Furthermore, it removes user bias based on interpretation of the observations recorded during 1F1, changing the plant model from a forensic reconstruction to an accident scenario under representative boundary conditions. In this analysis, the default time-at-temperature fuel rod failure model, described in greater detail in part II of this analysis, is activated [21].

2.2.2. Scenario Assumptions

Representative boundary conditions are preserved from the 1F1 plant model for the BSAF project and are shown in Table 4. As in the BSAF study for 1F1, gross creep failure of the lower head is assumed, and penetration failures are disabled. The decay heat and FP inventory boundary conditions used in this analysis are the same as those used in the BSAF plant model

[22]. Four periods of operation of the two train (A and B) isolation condenser (IC) are assumed. IC activity takes place from 0.10-0.28 hours for trains A and B, 0.52-0.55 hours for train A, 0.63-0.67 hours for train A, and 0.77-0.80 hours for train A. Each IC train is assumed to remove heat equal to 42.4 MW per train for the duration of operation. Minimal water injection is modeled during the first 25 hours of the scenario. A rapid linear increase in flow occurs between 9.20 and 9.21 hours from 0.0 kg/s to a maximum flow rate of 0.36 kg/s. The maximum allowable flow rate continues at 0.36 kg/s through the scenario, which is scaled based on the steam dome pressure. No flow is assumed when steam dome pressure is above 1.10 MPa, and maximum flow is assumed when steam dome pressure is 0.60 MPa. Injected water is assumed to reach the lower plenum until lower head failure occurs. After lower head failure, water is injected directly into the drywell cavity. Recirculation pump leakage to the drywell of the containment is assumed (approximately 10 gallons/min). Drywell head flange leakage from the containment drywell to the undershield plug is also assumed to occur starting at 0.648 MPa. Wetwell Venting at 23.7 hours and a reactor building explosion at 24.8 hours are also assumed.

Table 4. Boundary Conditions

Boundary Condition	**Description**
SRV Seizure	Not permitted
SRV Gasket Leak	Not permitted
Main Steam Line Rupture	Not permitted
Lower Head Gross Creep Failure	Permitted
Lower Head Penetration Failure	Not permitted
Drywell Head Flange leakage	Begins at 0.6481 MPa pressure in the drywell
Main Steam Line Isolation Valve Closure	At 0.0 hours
Feedwater System Ceases Operation	At 0.0 hours
IC Train A Operation	0.1-0.28 hours 0.52-0.55 hours 0.63-0.67 hours 0.77-0.8 hours
IC Train B Operation	0.1-0.28 hours
Wetwell Venting	At 23.7 hours
Reactor Building Explosion	At 24.8 hours

2.3. Comparison Methodology

In part I of this benchmark, baseline model behavior is examined through single case, best-estimate simulations using the interactive materials model and the eutectics model. Nominal values are used in both models for uncertain parameters (e.g. zirconium breakout temperatures, core component failure temperatures, candling parameters, etc.). Uncertainties associated with these parameters are investigated in more detail in part II of this benchmark: Material Interactions in Severe Accidents - Benchmarking the MELCOR V2.2 Eutectics Model on a BWR with Representative Fukushima Daiichi Boundary Conditions: Part II - Uncertainty Analysis. In this analysis, ZRO2-INT and UO2-INT liquefaction temperatures are equal to the SOARCA mean value, 2479 K, for the interactive materials model simulation. Proper

implementation of the interactive materials model requires that core component failure criteria be set equal to the same temperature to properly fail core structures. The single case, best-estimate simulations are analyzed and compared according to a similar methodology presented in the Modular Accident Analysis Program (MAAP)-MELCOR Crosswalk [23].

First, the overall accident progression is described in detail. This includes comparison of key accident signatures for each simulation. Key accident signatures are defined in this study as event timings indicative of deteriorating conditions in the core including decreasing water level, FPB failure, transitions between core damage states/accident phases, etc. Core energy functions are also compared to provide insight into dominant modes of energy production and loss, and their implications on core debris morphology.

Second, a comparison of hydrogen generation between the two simulations is made. Hydrogen is a highly combustible gas generated by the oxidation of core materials. Differences in the accident progression between the two simulations affect the available inventory of oxidant and the surface area exposed to the oxidant.

Next, a comparison is made of the thermal hydraulic response in both the primary system and containment. RPV water level, pressures, and temperatures in the primary system and containment provide additional context to the accident progression outlined in section 3.1 and the conditions in the primary system during peak in-core hydrogen production.

Finally, the fourth and fifth elements of this comparison – reactor core degradation and reactor pressure vessel lower head breach – interrogate the implications of both the interactive materials and eutectics models effects on core component degradation and failure, debris formation and morphology, and other aspects of in-vessel debris evolution. Figures of merit include intact component temperatures and mass fractions; core melt progression; debris morphology, distribution, and temperature; thermal challenge to the lower head; and ejected debris masses.

3. RESULTS AND DISCUSSION

The following section details an in-depth comparison between the interactive materials model and eutectics model simulated plant behavior. Plots have been annotated with vertical bands of blue, white, and red from left to right to illustrate the early in-vessel (up to the initial loss of rod-like geometry – defined in this study as the onset of candling), late in-vessel (up to initial lower head failure), and ex-vessel phases of each respective simulation. Results deviating from this format are explained as they are introduced. Interactive materials (e.g. ZRO2-INT) are denoted, in this section, an “-interactive” suffix.

3.1. Overall Accident Progression

A comparison of key event timings from a single simulation for each respective model are shown in Table 5. Strong agreement is observed in timings of early in-vessel phase events (e.g. core boiloff from top of active fuel (TAF) to bottom of active fuel (BAF)); time differences in the occurrence of all core boiloff phenomena are less than or equal to two minutes. Initial gap release occurs at 3.45 hours in both simulations, after significant core boiloff has occurred, the

core is less than 1/3 uncovered, during the early in-vessel accident phase. Strong agreement between simulations is typical for severe accident codes during the early in-vessel phase of accident progression in perturbation and sensitivity studies; the result of strong validation of relevant models, and limited degrees of freedom.

Table 5. Key Event Timings

Event	Interactive Materials model [h]	Eutectics Model [h]
Core Water Level at TAF	2.54	2.56
Core Water Level at 2/3 TAF	2.88	2.89
Core Water Level at 1/3 TAF	3.19	3.19
Core Water Level at BAF	4.00	3.97
Initial Gap Release	3.45	3.45
Initial Candling in Ring 1	3.69	3.64
Initial Particulate Debris Formation	3.64	3.70
Initial Core Plate Failure	5.05	5.01
Core Slump	5.25	5.01
Lower Plenum Dryout	7.56	6.36
Initial RPV Failure	10.72	8.34

Late in-vessel phase events included in Table 5, show strong agreement initially, but local differences are observed to evolve into large temporal differences in the occurrence of lower plenum dryout and initial RPV failure. This observation is also confirmed in Figure 3, which shows core degradation maps at various times in the scenario. Such differences in accident progression are a byproduct of increasing degrees of freedom that occurs by the introduction of previously inactive and/or nonexistent physical and phenomenological connections between core components and materials, i.e. late in-vessel phase severe accident phenomena and relocation of core materials. The onset of the late in-vessel accident phase is observed to occur at 3.64 hours, approximately three minutes earlier in the eutectics model simulation. It is noteworthy to observe that the occurrence of initial candling in ring 1 (the centermost core ring) and initial particulate debris formation are reversed between the two simulations. The eutectics model exhibits candling before particulate debris formation, whereas the interactive materials model simulation exhibits the opposite. These degradation pathways, candling and particulate debris formation, correspond to distinct debris relocation characteristics discussed in greater detail in part II of this analysis. Shortly after the onset of the late in-vessel phase, at four hours, accelerated degradation of core structures is observed (discussed in greater detail in section 3.4), as shown in Figure 3(b).

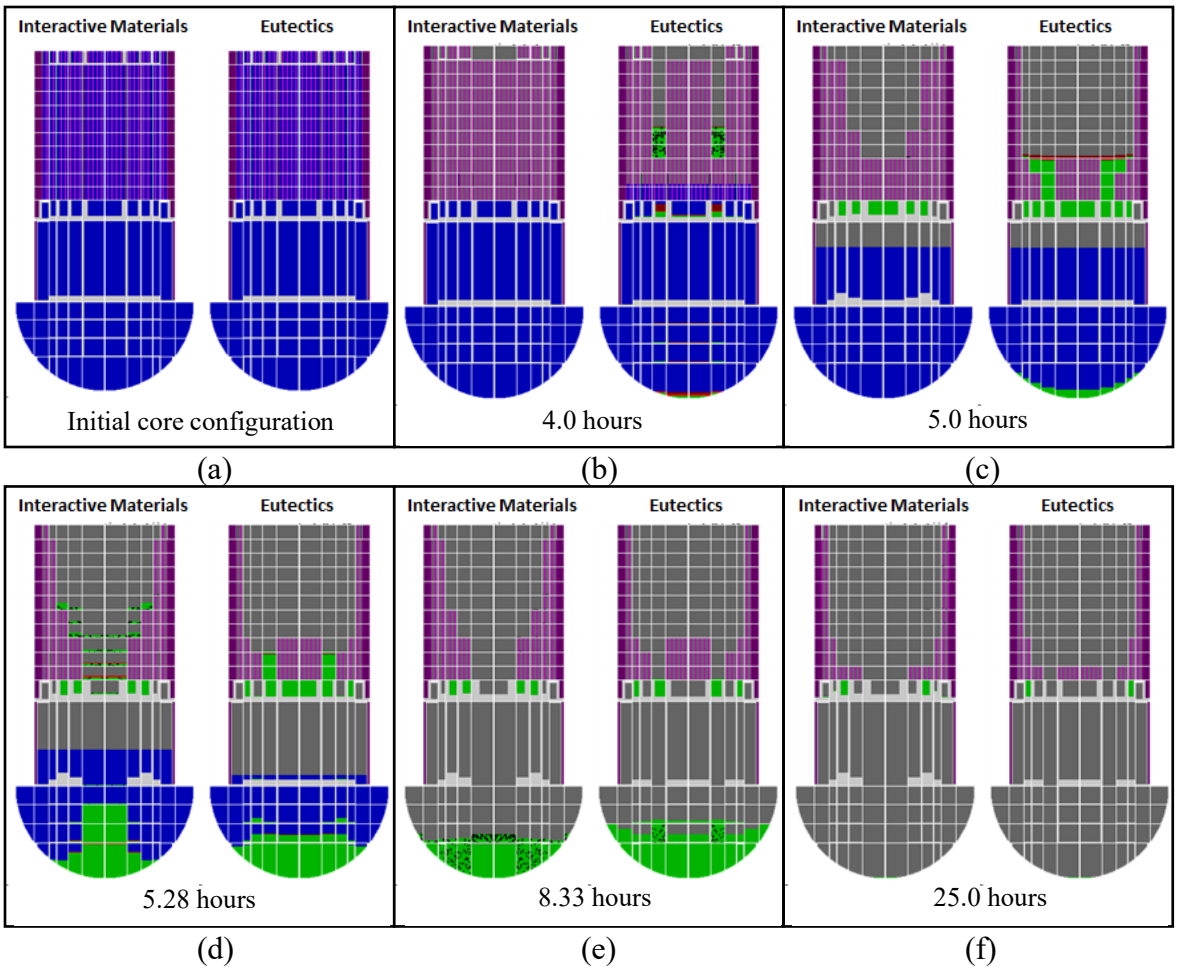

Figure 3. Core degradation maps over 25 hours (a) initial core configuration, (b) 4.0 hours core degradation map, (c) 5.0 hours core degradation map just before core plate failure, (d) 5.28 hours core degradation map after core slumping has occured, (e) 8.33 hours core degradation map just before lower head failure in the eutecitcs model simulation, (f) 25 hours core degradation map

Core plate failure marks a major transition within the late in-vessel accident phase, creating a pathway for massive debris relocation to the lower plenum. In both simulations, core plate failure is observed to occur just after five hours (Figure 3(c)); the eutectics model simulation exhibits core plate failure 3 minutes earlier than the interactive materials model simulation. The eutectics model simulation exhibits core slumping, defined as relocation of 20% of the initial fuel mass to the lower plenum, at the same time as core plate failure. Conversely, the interactive materials model simulation exhibits a 12 minute delay between core plate failure and core slumping. The core degradation map after core slumping in both simulations is shown in Figure 3(d). Debris accumulation in the lower plenum boils the remaining water inventory. Lower plenum dryout occurs at 6.36 hours, approximately 1.5 hours after core plate failure, for the eutectics model simulation. The interactive materials model simulation exhibits delayed lower plenum dryout, approximately 1.2 hours longer, at 7.56 hours. Figure 3(e) shows that the eutectics model exhibits more complete destruction of core structures at 8.33 hours, just before lower head failure in the eutectics model.The eutectics model exhibits lower head failure at 8.34 hours, 2.38 hours before the interactive materials model simulation, which exhibits lower head failure at 10.72

hours. Key accident signatures are consistently simulated to occur at later times for the interactive materials model simulation when compared to the same accident signatures simulated by the eutectics model simulation. Figure 3(f) shows that after 25.0 hours, both simulations exhibit comparable core damage.

3.2. Hydrogen Generation

The amount of energy released by the oxidation of core materials is proportional to the amount of hydrogen liberated; ~6.5 MJ are released per kg of hydrogen generated. Figures of merit corresponding to hydrogen generation for each simulation are illustrated in Figure 4 and Figure 5, which show the distribution of hydrogen generation by material and radial location, respectively.

It is observed in Figure 4, that hydrogen is generated primarily by the oxidation of zirconium-based structures (fuel cladding and canister wall), while minimal hydrogen is produced by B_4C reactions. Similar quantities of hydrogen are produced by B_4C reactions in both simulations. The interactive materials model simulation, however, exhibits greater hydrogen generation from the oxidation of both stainless steel and zirconium-based structures than the eutectics model simulation. As discussed in sections 3.1 and 3.4, the eutectics model simulation exhibits earlier failure of core components, including fuel and cladding components. Conversely, in the interactive materials model simulation, components remain above the core plate, in an oxidizing steam environment, for a longer period of time. In other words, earlier relocation of large quantities of debris to the lower plenum, as observed in the eutectics model simulation, limits the degree of oxidation of core materials that can take place. At the end of the simulation, 25 hours, the interactive materials model exhibits 761 kg of hydrogen, about 145 kg more than the eutectics model simulation's 615.7 kg of hydrogen.

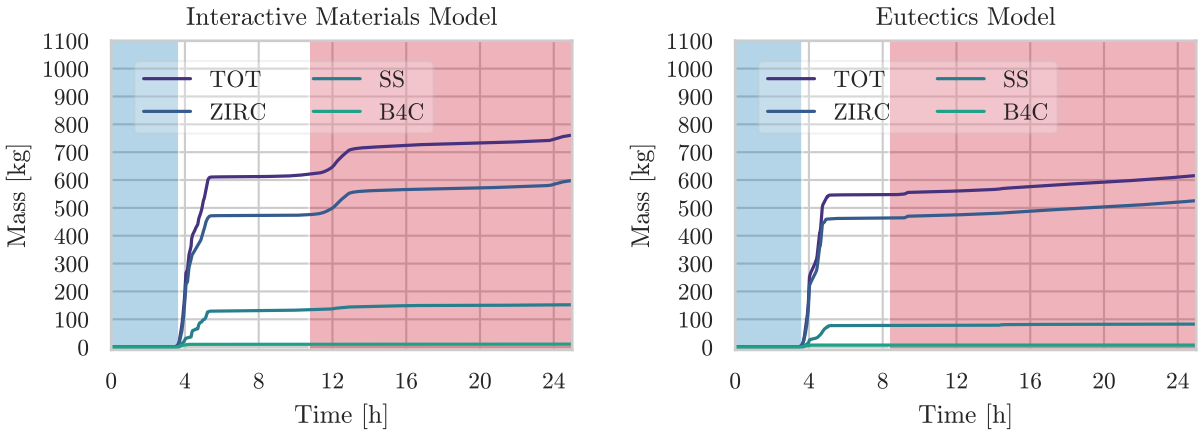

Figure 4. Comparison of hydrogen generation by material.

For both the interactive materials model simulation and the eutectics model simulation, hydrogen production begins in the innermost rings (1, 2, and 3) at nearly the same time, followed by ring 4, and finally ring 5 as shown in Figure 5. For the interactive materials model simulation, the majority of hydrogen production occurs between (3.5-6 hours) during core and lower plenum

boiloff. The primary hydrogen generating transient occurs in the eutectics model simulation during the same time period. At 25.0 hours, the interactive materials model simulation exhibits between 13 kg and 56 kg more hydrogen generation in each core ring in comparison to the eutectics model simulation. This observation is consistent with earlier observations that core components, fuel components in particular, remain intact for longer periods in the interactive materials model simulation. The greatest differences in hydrogen generation are observed in rings 2 and 5. In ring 2, fuel and cladding components are observed to completely fail before 5 hours in the eutectics model simulation, preventing continued oxidation of those materials. In ring 5, the interactive materials model simulation exhibits elevated core temperatures, in excess of 1500 K, promoting greater hydrogen generation.

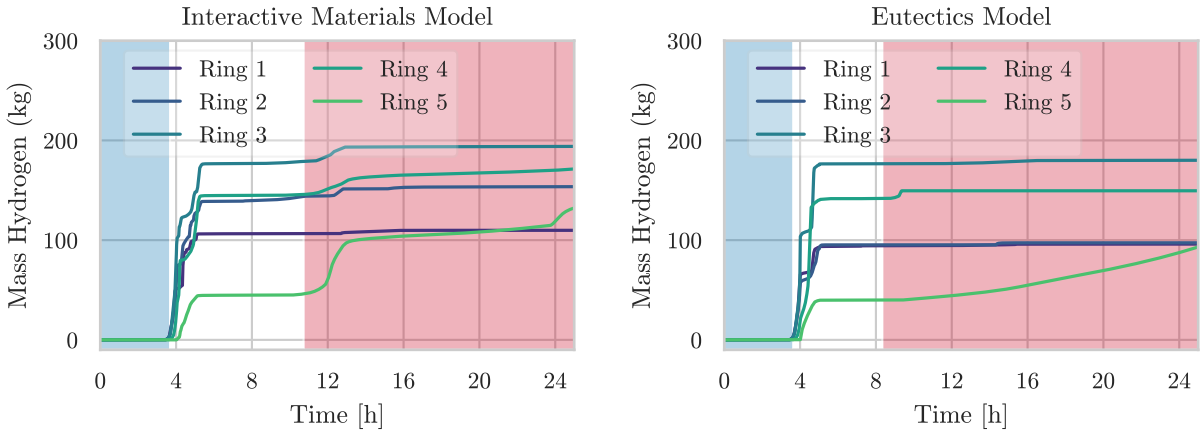

Figure 5. Comparison of hydrogen generation distribution.

3.3. Thermal Hydraulic Response

3.3.1. Primary Coolant System Response

The RPV steam dome pressure transient for each simulation is shown in Figure 6. An initial decrease in steam dome pressure is observed at the beginning of both simulations (0.0 - 0.28 hours) when both IC trains are operating. After IC train B ceases operation at 0.28 hours, however, RPV steam dome pressure increases to the SRV opening setpoints. At 0.8 hours, IC train A shuts off for the remaining duration of the accident scenario and no further core cooling is provided by either train of the IC system. SRV cycling continues through the early and late in-vessel phases of the accident until primary system depressurization by lower head failure in both models; for approximately 9.9 hours in the interactive materials model simulation, and 7.5 hours in the eutectics model simulation. The interactive materials model simulation exhibits less frequent SRV cycling after lower plenum and downcomer dryout, but prior to lower head failure, due to steam starvation and the lack of coolant inventory available to vaporize. The same behavior is not observed in the eutectics model simulation because downcomer dryout does not occur before lower head failure. After lower head failure, primary system pressure follows closely that of containment pressure in both simulations.

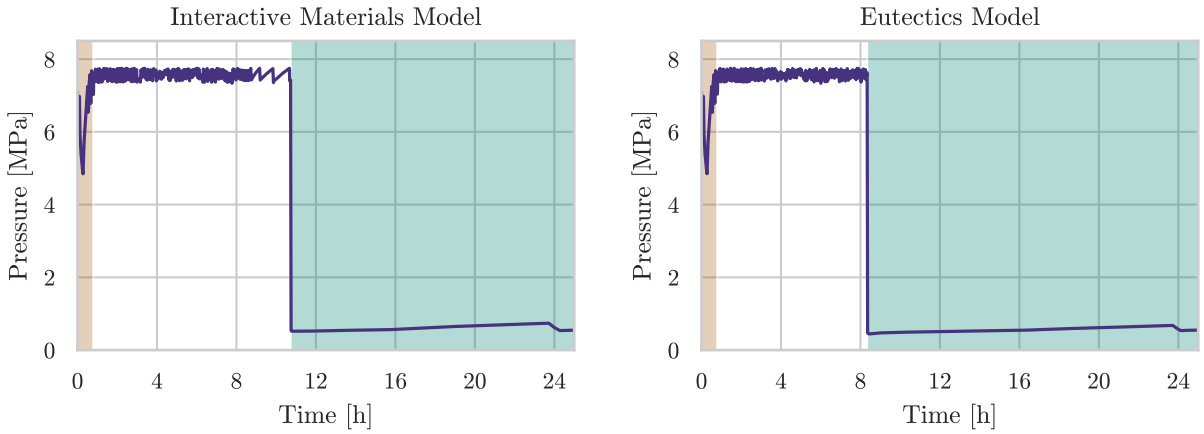

Figure 6. Comparison of the RPV pressure transient. Vertical bands highlight periods of IC operation (0.0-0.8 hours), sustained SRV cycling (~0.8 - lower head failure), and post-lower head failure (lower head failure - 25 hours), respectively.

Figure 7 shows the temperature transient in the RPV steam dome. Near the end of the early in-vessel phase, steam dome temperatures begin to rise due to core uncovery and associated steam production. Shortly after the onset of the late in-vessel phase, at approximately 4.0 hours, both models exhibit rapidly rising temperatures in the steam dome, coincident with rapid hydrogen generation by highly exothermic oxidation of core materials by steam. The rapid rise in steam dome temperature is interrupted when the RPV water level drops below BAF due to a decrease in the steam production, as shown in Figure 8. Both simulations exhibit a second peak in steam dome temperatures coincident with renewed oxidation of core materials by steam associated with lower plenum boiloff. Lower plenum boiloff begins after core plate failure for interactive materials model simulation. Conversely, the eutectics model simulation exhibits renewed lower plenum boiloff and increasing steam dome temperatures in combination with debris relocation to the lower plenum (discussed in section 3.5) prior to core plate failure. After lower plenum boiloff has occurred, steam dome temperatures are observed to increase in a pseudo-linear fashion in both simulations, with small features corresponding to debris relocation and SRV activation, until lower head failure. After an initial, sharp decrease in steam dome temperature coincident with lower head failure, steam dome temperatures increase as remaining core components, particularly in outer core rings, oxidize further. Peak steam dome temperatures observed for both simulations over the course of the transient occur during core slumping and are 1246 K for the interactive materials model simulation and 1123 K for the eutectics model simulation.

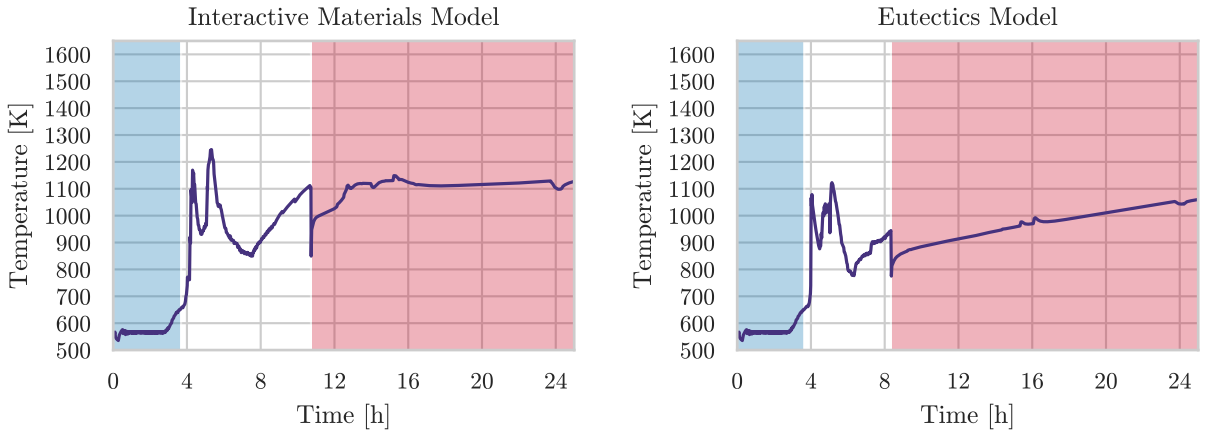

Figure 7. Comparison of the steam dome temperature transient.

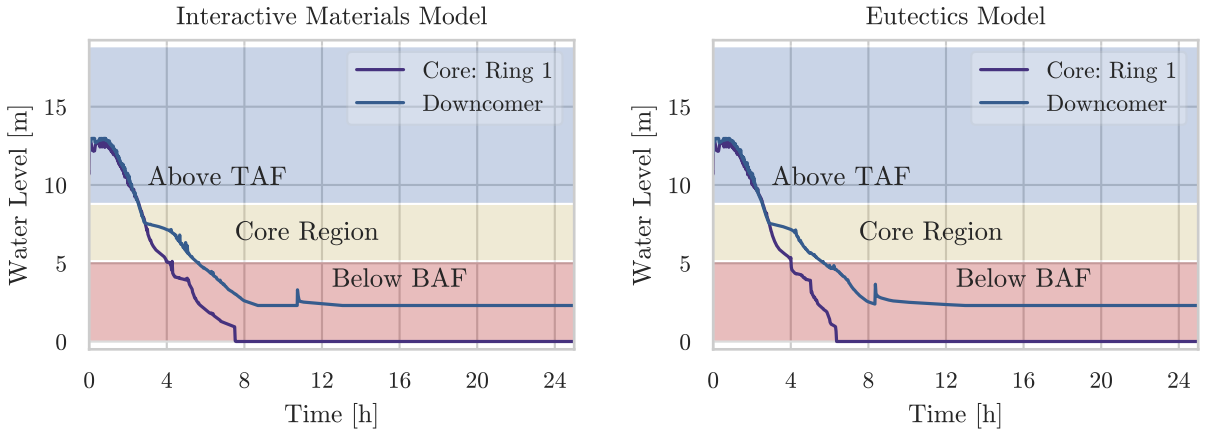

Figure 8. Comparison of the RPV water level transient.

RPV water level is shown in Figure 8. As with other figures of merit thus far considered, little difference is observed between the simulations until the late in-vessel phase begins, when the core water level is near the BAF. Lower plenum dryout occurs 2.51 hours after core plate failure for the interactive materials model simulation, and 1.35 hours after core plate failure for the eutectics model simulation. Lower plenum boiloff is observed to be more rapid in the eutectics model simulation because of more significant debris relocation to the lower plenum. In both simulations, downcomer water level trails core water level until the top of the jet pump is reached, at which point it decreases more slowly to the bottom of the jet pumps. Lower head failure causes a small peak in downcomer water levels in both simulations due the accompanying change in pressure.

3.3.2. Containment Response

Figure 9 and Figure 10 show pressures in the drywell and wetwell, respectively. In both simulations, the wetwell pressure follows very closely the drywell pressure. During the early in-vessel phase, SRV cycling has little effect on containment pressure because the steam is injected

into the suppression pool, where it condenses. After the late in-vessel phase begins, near 4.0 hours in both simulations, drywell and wetwell pressures rise in response to the addition of noncondensable gases (NCGs); hydrogen that is generated rapidly in the core region in both simulations and is transported into containment by SRV cycling. Both simulations exhibit a gradual increase in containment pressure after the termination of the hydrogen generating transient up until lower head failure. As can be seen in Figure 11, the suppression pool does not reach saturation temperatures in either simulation. In other words, the suppression pool does not boil. Thus, pressure changes in containment are driven by the transfer of hot noncondensable gases in the primary system to containment until lower head failure in both simulations.

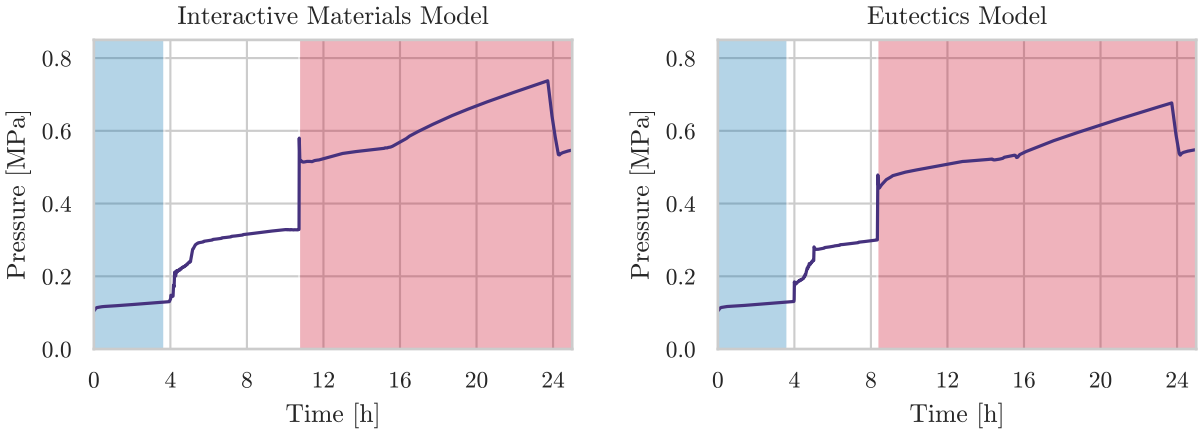

Figure 9. Comparison of the drywell pressure transient.

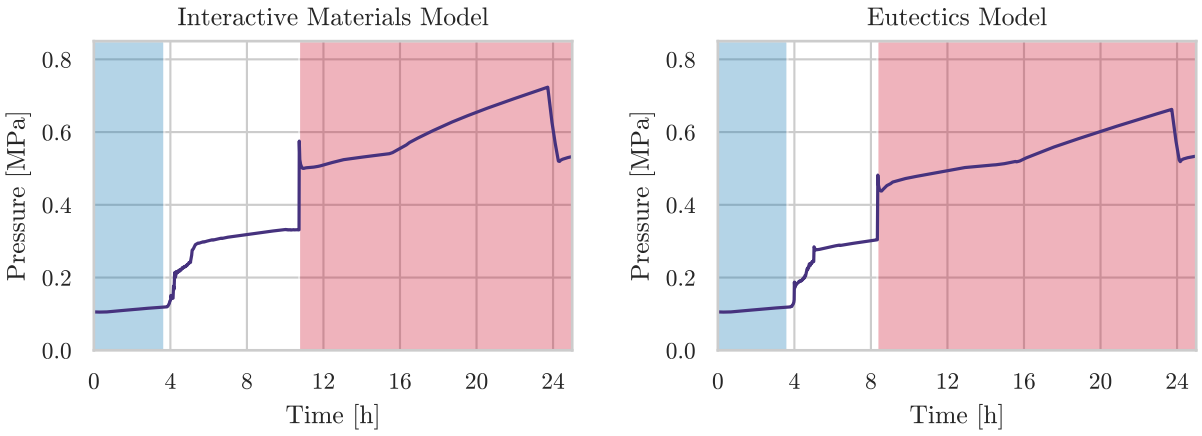

Figure 10. Comparison of the wetwell pressure transient.

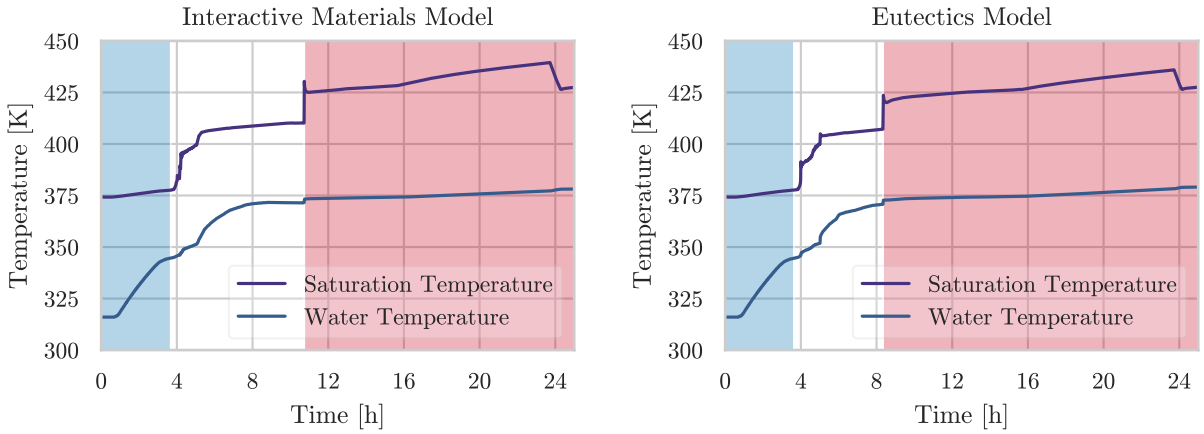

Figure 11. Comparison of the suppression pool temperature transient.

Lower head failure causes drastic pressurization of containment (> 0.15 MPa change) in both simulations due to the liberation of remaining inventories of NCGs and steam flashing of water from the primary system to containment. After the initial pressurization event, containment pressures are observed to decrease initially, likely as a result of steam condensation. In both simulations, containment pressures then continue to increase due to containment heatup and continued NCG production until containment venting at 23.7 hours.

3.4. Reactor Core Degradation

After the onset of the late in-vessel phase of core degradation begins, changes to core geometry and debris formation occurs quickly. Figure 12 shows the core melt progression for both simulations. Within the first hour of the late in-vessel phase, molten debris masses reach between 10-20 Mg for both simulations. Greater peak molten masses are observed in the eutectics model simulation in both the active core region and lower plenum region. Molten material is more persistent and masses are greater in the active core region than the lower plenum region for both simulations. By about 6 hours, the molten debris in both simulations has refrozen completely, and remains solid until lower head failure. After lower head failure, both simulations exhibit molten material formation in the active core region. The interactive materials model exhibits the formation of a small, persistent mass of molten material shortly after lower head failure that remains until the end of the accident scenario at 25 hours. The maximum mass attained by the molten material is 2.0 Mg, which decreases to >0.2 Mg near 16 hours. Conversely, a single, short-lived instance of molten material formation in the active core region is observed after lower head failure for the eutectics model simulation.

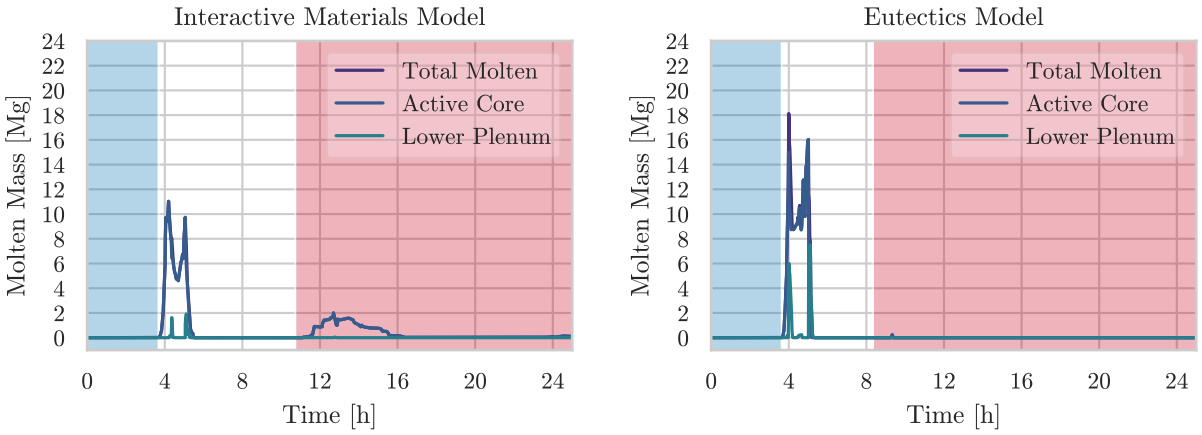

Figure 12. Comparison of the core melting progression.

Molten pools form when core debris is blocked from relocating further downward in the core, and temperatures exceed material melting points. Figure 13 shows the minimum axial flow area in each core ring. Each instance of large molten material masses coincides with decreased axial flow area. In particular, maximum molten material masses coincide with complete blockages of one or more core rings. When a blockage forms, coolant can no longer move through a core ring, and energy is no longer convected away from the debris, promoting molten material formation. Normalized axial flow areas can exceed 1.0 when intact core components fail, increasing the axial flow area beyond its original value. The interactive materials model simulation exhibits persistent blockages in rings 2-5, whereas the eutectics model simulations only exhibits a persistent blockage in rings 4 and 5. Reduction of axial flow area can be the result of either buildup of particulate debris or flow path occlusion by candled materials. For example, the flow area reduction in rings 2 and 3 observed during the ex-vessel phase of the interactive materials model simulation are coincident with particulate debris buildup in the active core region (not shown). Furthermore, both simulations exhibit axial flow areas that increase beyond the original value. For the interactive materials model simulation, the axial flow area is increased beyond the original value only in ring 1. Conversely, the eutectics model exhibits increased axial flow areas in rings 1-3. The effects of reduced axial flow are also observed in the hydrogen generation and the steam dome temperature transients in Figure 5 and Figure 7, respectively.

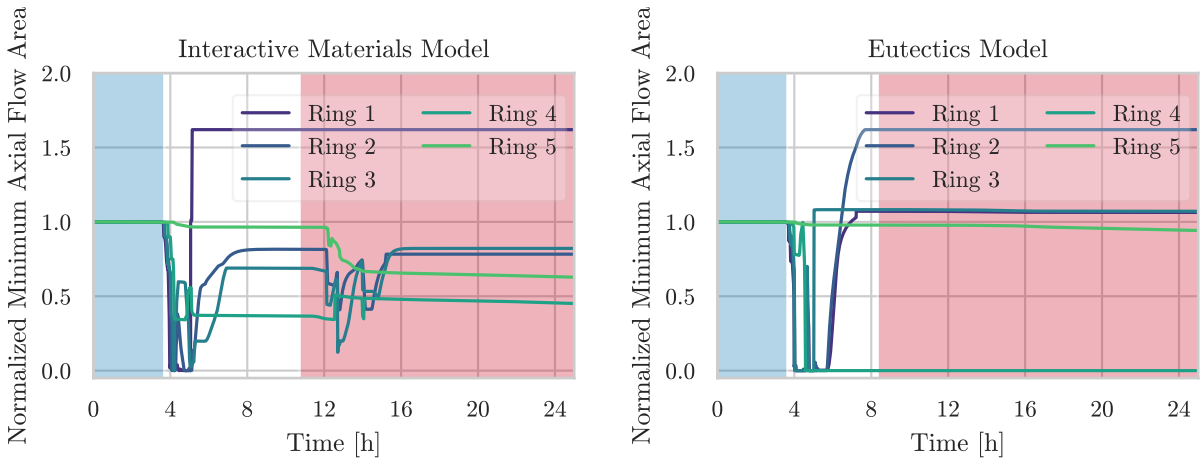

Figure 13. Comparison of the minimum axial flow area through the active core region.

Control rod poison (CRP) structure temperature transients and intact mass fractions are shown in Figure 14 and Figure 15, respectively. Early, complete destruction of CRP structures are observed in rings 1-4 by 5 hours for both simulations. After lower head failure, CRP structures are observed to fail in ring 5 for the interactive materials model simulation, but not in the eutectics model simulation. The temperature of B_4C in all core cells containing intact CRP structures[6] are shown in Figure 14. Both simulations exhibit CRP heat-up beginning in the early in-vessel phase to each respective B_4C /stainless steel parametric failure temperature; 1520 K for the interactive materials model simulation and 1700 K for the eutectics model simulation. Standard practice to capture the B_4C /stainless steel interaction in CRP structures when using the interactive materials model is to fail those components parametrically at the eutectic temperature (1520 K). Conversely, the eutectics model captures the B_4C /stainless steel interaction only after component temperatures exceed the eutectic temperature; thus, the parametric failure temperature is set above the eutectic temperature at 1700 K in this analysis. Figure 15 shows the corresponding degradation of CRP structures. Both simulations exhibit complete destruction of CRP structures in rings 1-4 and 10% degradation of structures in ring 5 by 5 hours. In the interactive materials model simulation, CRP structures remaining in ring 5 have failed by 13 hours, coincident with significant hydrogen production by oxidation of Zr-based structures in ring 5. For the eutectics model simulation, no degradation of ring 5 CRP structures is observed after 5 hours.

[6] When an intact component has a mass of 0.0 kg in MELCOR (i.e. the component has failed or was initialized without mass), that component temperature is set equal to 0.0 K.

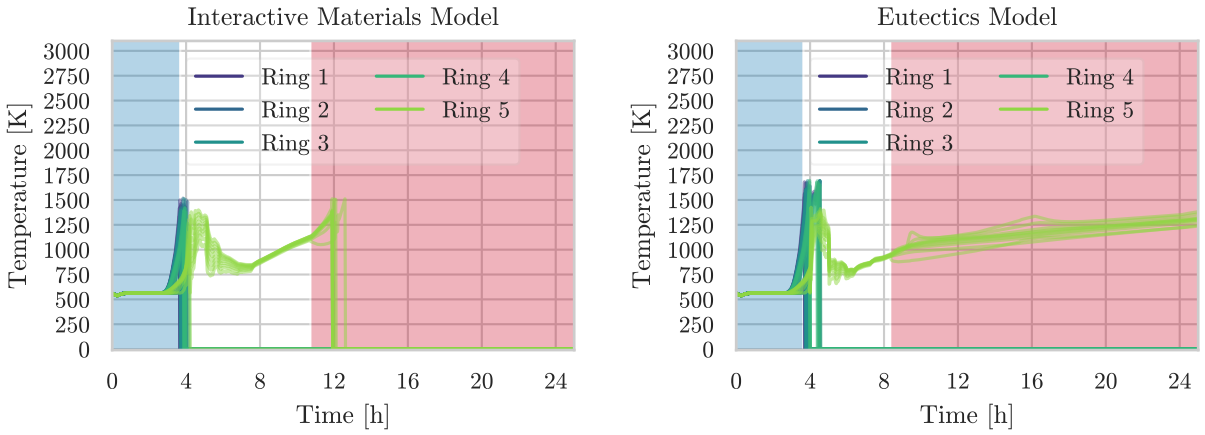

Figure 14. Comparison of control blade poison temperatures.

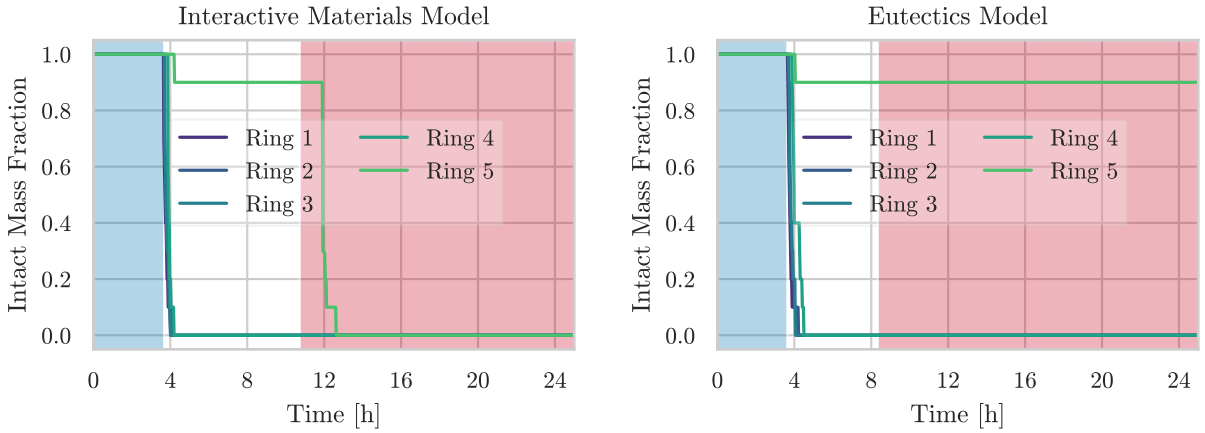

Figure 15. Comparison of control blade damage progression.

Fuel canister temperatures for both models exhibit similar qualitative behavior to CRP temperatures and are shown in Figure 16. Rapid heat-up is observed at the end of the early in-vessel phase during core boiloff reaching parametric failure temperatures of 2100 K (Zr melting point) by 5 hours. After rapid heatup and degradation, during lower plenum boiloff, remaining fuel canister components undergo significant cooling. Fuel canister temperatures decrease to between 650 K and 1000 K, with the eutectics model simulation exhibiting lower temperatures than the interactive materials model simulation. Following lower plenum dryout, fuel canister temperatures rise in both simulations. The second period of fuel canister heatup is more significant for the interactive materials model simulation, with some fuel canister components reaching the failure temperature setpoint around 12 hours due to increased exothermic oxidation of Zr-based components in ring 5. The eutectics model simulation does not exhibit fuel canister heatup beyond 1500 K, or any further failure of fuel canister components. Fuel canisters, a zirconium-based structure, are highly impacted by elevated temperatures because of the potential for runaway zirconium oxidation.

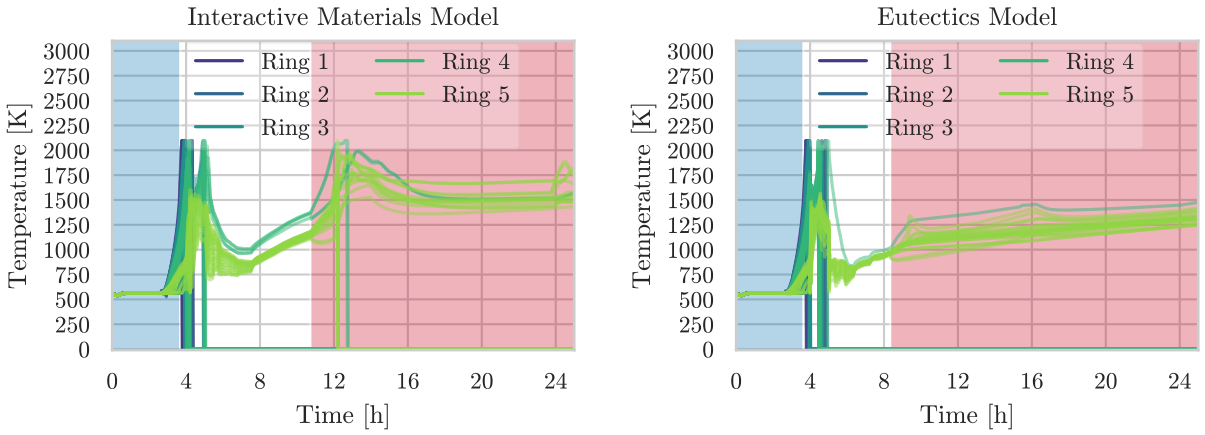

Figure 16. Comparison of fuel canister temperatures.

Complete destruction of fuel canister components in rings 1-3 is observed by 5 hours in both simulations. As temperatures rise towards the end of the late in-vessel phase and into the ex-vessel phase, further degradation of remaining fuel canister components is observed. Figure 17 shows that shortly after 5 hours, the interactive materials model still has intact components remaining in rings 4 and 5; 15% intact and 91% intact, respectively. For the eutectics model simulation, intact components are also remaining in rings 4 and 5; 5% intact and 92% intact, respectively. Near 12 hours, the interactive materials model simulation exhibits a reduction of intact mass by oxidation in rings 4 and 5. Further reduction of intact fuel canister mass through oxidation is also observed in ring 5 during the ex-vessel phase for the eutectics model simulation, but to a lesser extent. After 25 hours intact mass remains in rings 4 and 5 for both simulations. In ring 4, 5% of the original mass remains intact, while for ring 5, the interactive materials model shows significantly more degradation, 35%, than the eutectics model simulation, 77%.

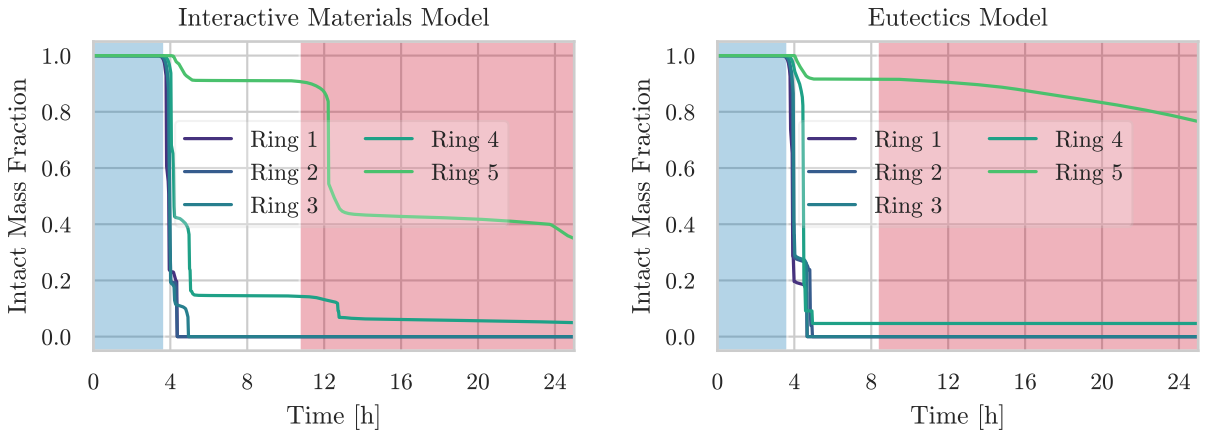

Figure 17. Comparison of fuel canister damage progression.

The fuel cladding, also zirconium-based, exhibits a similar initial heat-up profile in both simulations, as shown in Figure 18. Contrary to the observed fuel canister behavior, unoxidized

zirconium in the cladding superheats in excess of its melting point due to holdup by the oxide scale formed during cladding oxidation. Furthermore, a larger number of fuel cladding components remain standing after 5 hours in both simulations. Peak fuel cladding temperatures reach 2478.6 K in the interactive materials model simulation – the modified liquefaction temperature of UO_2-interactive and ZrO_2-interactive is set to 2479 K – and 2712.1 K in the eutectics model simulation during the late in-vessel phase. As with other core components, fuel cladding temperatures decrease during lower plenum boiloff. After lower plenum boiloff, temperatures increase steadily until lower head failure. During the ex-vessel phase of the accident, fuel cladding heat-up is observed to accelerate in multiple core cells, peaking between 2300 K and 2400 K in both simulations. Fuel cladding failures are also observed during the ex-vessel phase, at between 12 and 14 hours for the interactive materials model simulation and near 16 hours for the eutectics model simulation.

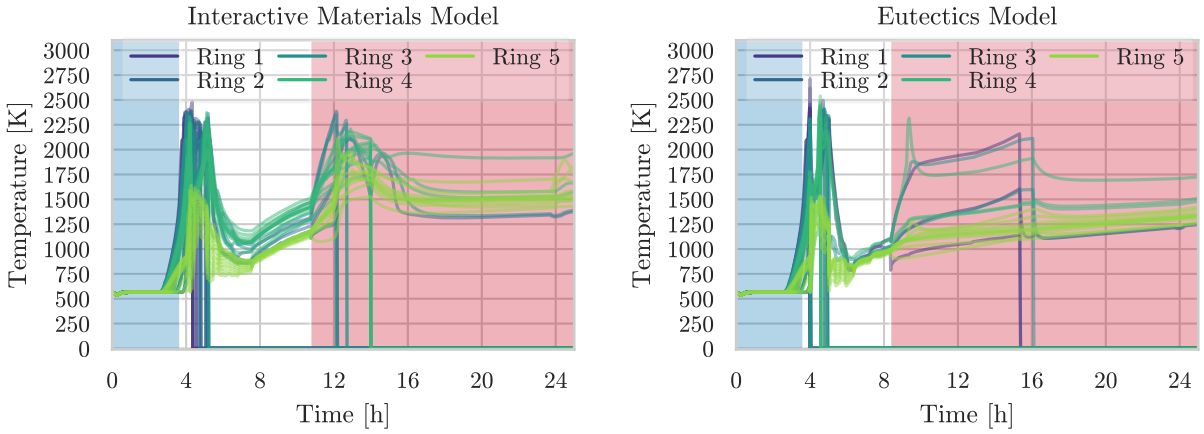

Figure 18. Comparison of fuel cladding temperatures.

Figure 19 shows the intact mass fractions for fuel cladding components in each ring of both simulations. Only partial degradation of the fuel cladding in rings 2-5 occurs in the interactive materials model simulation. At 5.5 hours, complete destruction of ring 1 cladding components has occurred in the interactive materials model simulation. Partial degradation in rings 2, 3, 4, and 5 has occurred, with 12%, 21%, 17%, and 85% remaining intact, respectively. After 25 hours, the same intact mass fractions have decreased to 12%, 12%, 13%, and 51%. Degradation of the fuel cladding is more significant for the eutectics model simulation In the eutectics model simulation, complete destruction of ring 2 cladding components has occurred by 5.5 hours. At the same time, 2%, 3%, 17%, and 86% of the original mass of Zr remains intact in rings 1, 3, 4, and 5. At 25 hours, remaining intact mass fractions are 1%, 1%, 11%, and 62%.

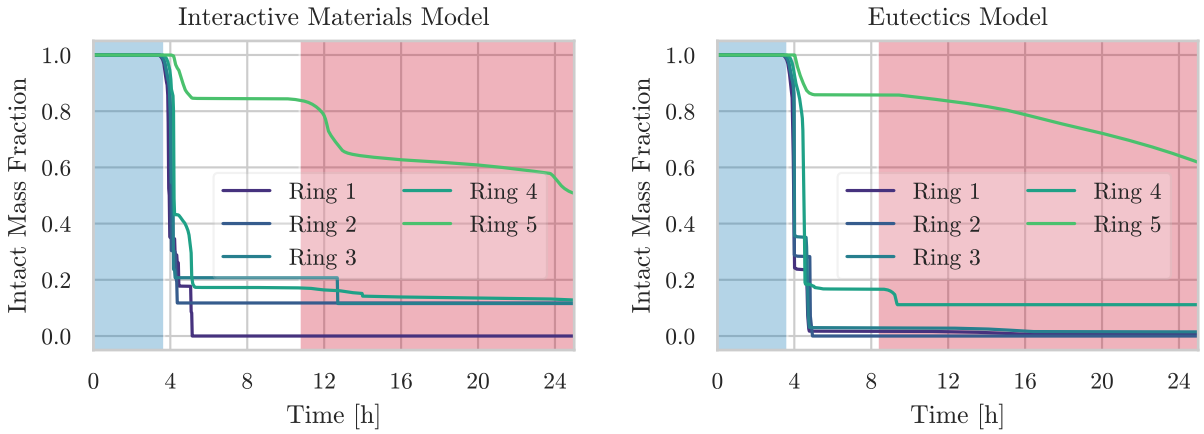

Figure 19. Comparison of fuel cladding damage progression.

Figure 20 and Figure 21 show intact fuel temperatures and intact fuel mass fractions, respectively. Fuel temperatures follow very closely, those observed for fuel cladding. Namely, heat-up begins towards the end of the early in-vessel phase. By 5 hours, peak temperatures reach 2479.0 K and 2928.1 K for the interactive materials and eutectics model simulations, respectively. As observed for other core components, fuel components cool during lower plenum boiloff and begin to heat up again after boiloff is complete. After lower head failure, multiple core cells are observed to fail, between 12-14 hours for the interactive materials model simulation, and near 16 hours for the eutectics model simulation. Intact mass fractions of fuel components, however, differs greatly from that of the cladding. In both simulations, partial degradation of fuel components is observed in rings 1-4, while ring 5 fuel components remains 100% intact after 25 hours. At 5.5 hours, rings 1, 2, and 3 have been significantly degraded (0%, 30%, and 50% remain intact) while ring 4 has only slightly degraded (99% remain intact) for the interactive materials model simulation. By 25 hours, fuel components in rings 2, 3, and 4 have undergone further degradation with 10%, 10%, and 30% of the original UO2 mass remaining intact, respectively. By comparison, the eutectics model simulation exhibits enhanced degradation of fuel components by 5.5 hours: 18%, 0%, 18%, and 25% of fuel components remain intact in rings 1, 2, 3, and 4, respectively. The same holds true at 25 hours, with 9%, 9%, and 25% of the original fuel components remaining intact in rings 1, 3, and 4, respectively.

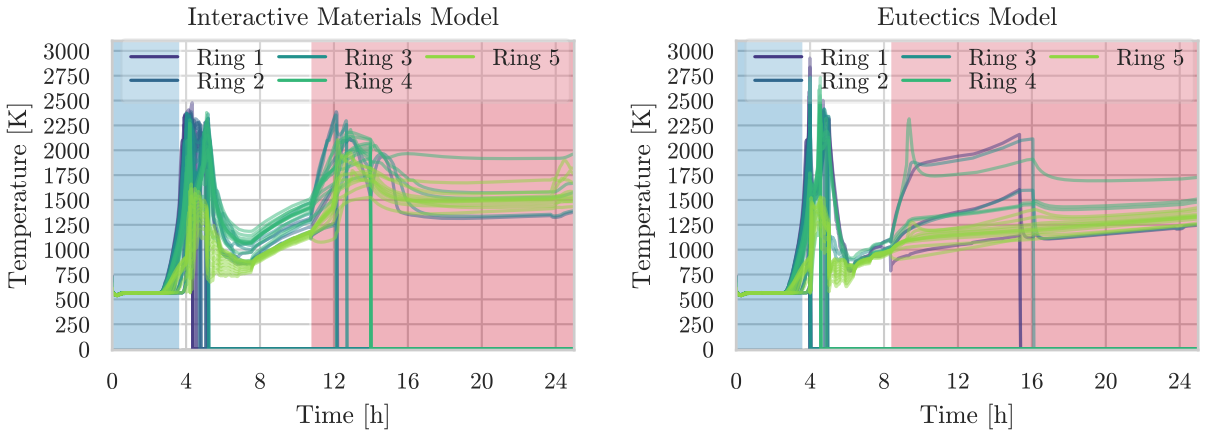

Figure 20. Comparison of fuel temperatures.

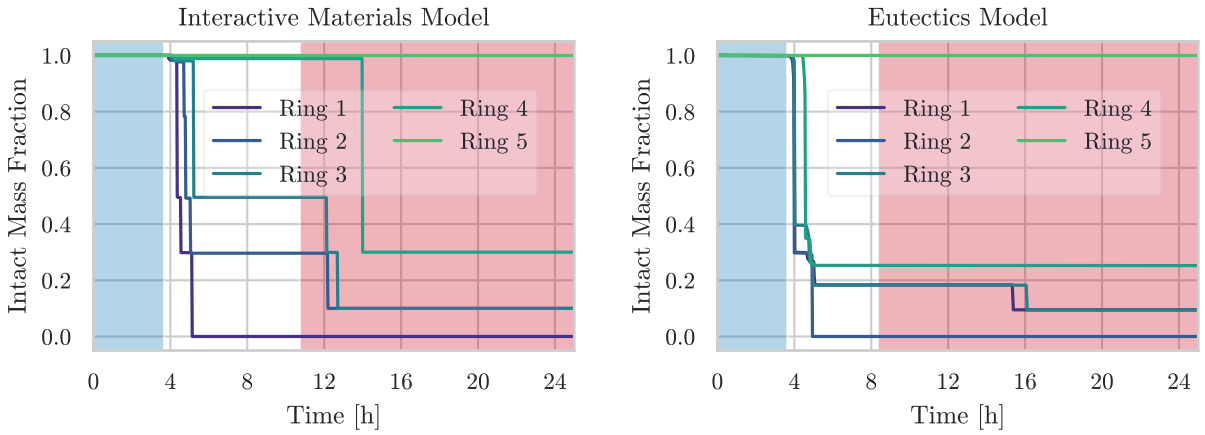

Figure 21. Comparison of fuel damage progression.

3.5. RPV Lower Head Breach

As follows from Figures 15-21, the interactive materials model simulation calculates smaller debris masses throughout the late in-vessel phase than the eutectics model, which is shown in Figure 22. The total mass of core materials is observed to increase in both simulations because of core material oxidation. Both simulations exhibit debris relocation to the lower plenum before core plate failure, however, the majority of debris is observed to build up on the core plate until its failure in both cases. Zr is observed to relocate to the lower plenum first in the interactive materials model, while in the eutectics model the first material to relocate to the lower plenum is stainless steel, quickly followed by B_4C (not shown). After core plate failure and termination of debris slumping, both simulations exhibit between 2-4 Mg of debris remaining in the core region. Maximum total debris masses in the RPV exhibited by the eutectics model simulation, 94.1 Mg, are larger than those exhibited by the interactive materials model simulation, 57.4 Mg. Furthermore, the eutectics model exhibits larger conglomerate debris masses. At the time of maximum debris masses, only 17.7 Mg of the total debris mass is made up of conglomerate debris (previously molten) in the interactive materials model simulation. By comparison, 58.1

Mg of the total debris is made up of conglomerate in the eutectics model simulation, more evidence of the greater tendency by the eutectics model to produce molten debris. At the time of lower head failure, the majority of debris is ejected; however, debris ejection events do occur until almost 16 hours in both simulations. The total mass of all materials remaining in the RPV after 25 hours are 84.8 Mg (8.3 Mg debris) for the interactive materials model simulation and 72.7 Mg (8.0 Mg debris) for the eutectics model simulation.

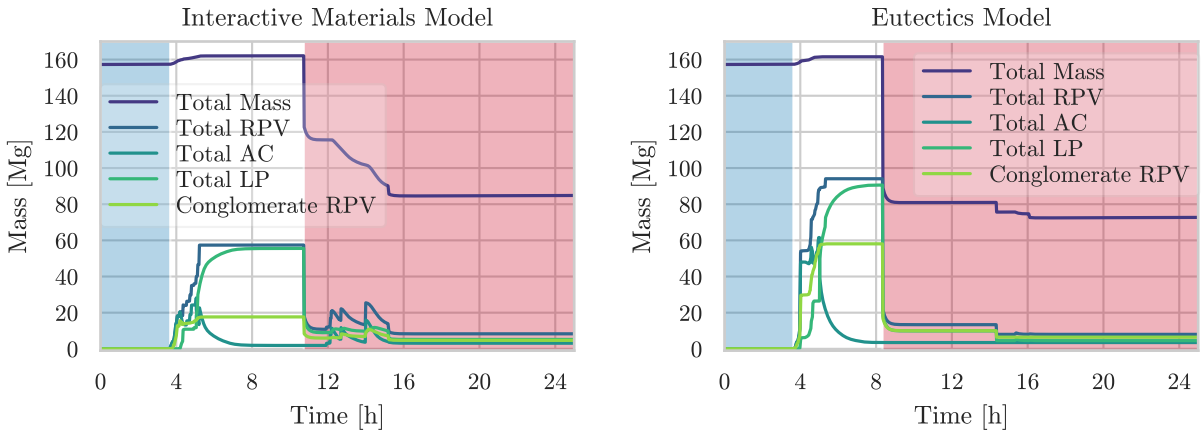

Figure 22. Comparison of debris mass distribution. Total Mass: total mass of all materials **(intact and debris)** in the RPV, Total RPV: total **debris mass** (conglomerate and particulate) in the RPV, Total AC: total **debris mass** (conglomerate and particulate) in the active core, Total LP: total **debris mass** (conglomerate and particulate) in the lower plenum, and Conglomerate RPV: total **conglomerate debris mass** in the RPV.

Both simulations exhibit lower plenum debris primarily made up of particulate debris, as shown in Figure 23. Oxidic and metallic molten pools (MP1 and MP2) exist only for a short period of time during initial relocation to the lower plenum. In fact, shortly after core slumping to the lower plenum, all of the molten debris, including conglomerate particulate debris above its melting point, refreezes in both simulations as discussed earlier (see Figure 12 and associated discussion). A significantly larger particulate debris bed is observed in the eutectics model simulation with a mass of 90.6 Mg. Of that mass, 55.1 Mg, or 60.8%, is conglomerate debris and was previously molten. By comparison, the interactive materials model particulate debris bed is calculated to be 55.6 Mg, with 17.2 Mg, 30.9%, of previously molten conglomerate debris. The larger mass of hot debris accelerates boil-off of the lower plenum, discussed above, and presents an earlier thermal challenge to the lower head.

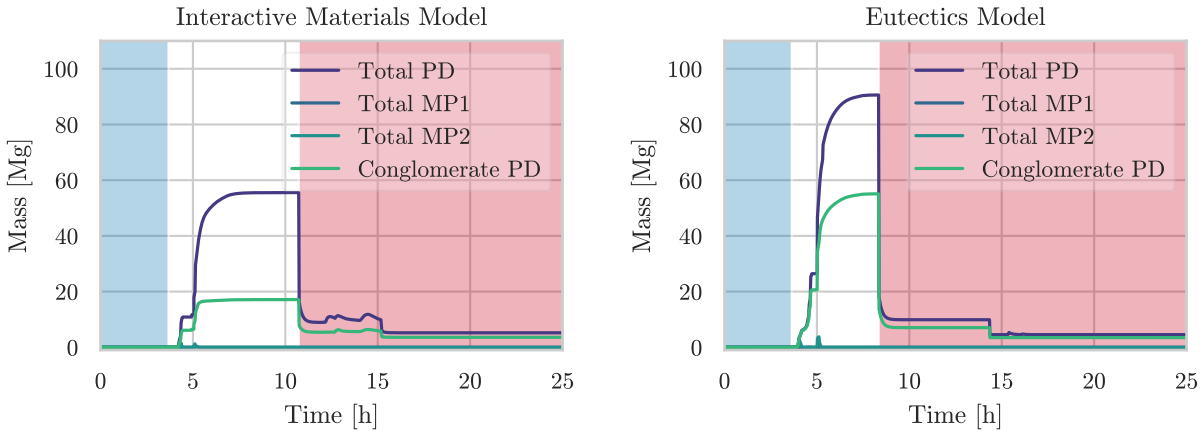

Figure 23. Comparison of lower plenum debris masses.

Figures 24-26 show the lower plenum debris temperatures in all lower plenum core cells for each debris component type (particulate debris, oxidic molten pool, and metallic molten pool). Peak lower plenum debris temperatures are higher in the eutectics model simulation. Furthermore, debris arrives in the lower plenum earlier in the eutectics model simulation, within minutes of the onset of candling, though both simulations exhibit debris in the lower plenum within 0.5 hours of the start of the late in-vessel phase. During the late in-vessel phase, peak particulate debris, oxidic molten pool, and metallic molten pool temperatures reach 2213.6 K, 2156.9 K, and 2153.9 K, respectively in the interactive materials model simulation. In the eutectics model simulation, peak temperatures are higher; PD, MP1, and MP2 temperatures reach 2654.4 K, 2872.8 K, and 2236.3 K, respectively. During the ex-vessel phase, however, average PD temperatures peak higher in the interactive materials model simulation, consistent with the larger proportion of heat-bearing materials remaining as an energy source in the RPV after lower head failure. The same also holds true for MP1 and MP2 temperatures.

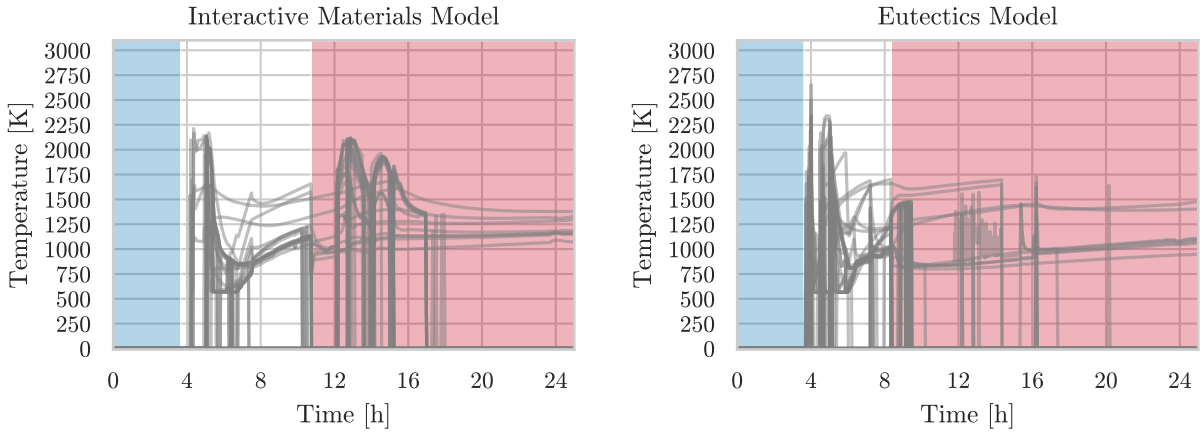

Figure 24. Comparison of particulate debris temperatures.

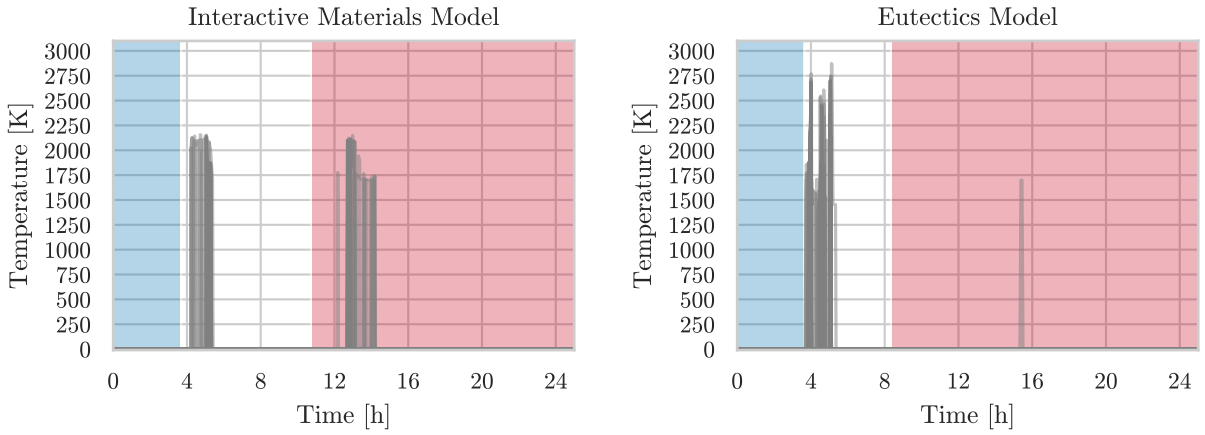

Figure 25. Comparison of oxidic molten pool temperatures.

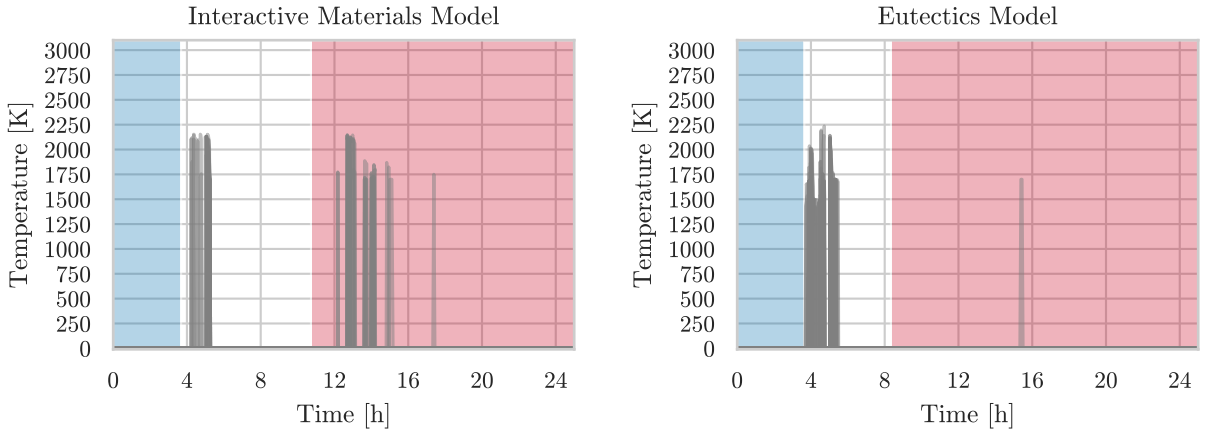

Figure 26. Comparison of metallic molten pool temperatures.

As stated previously, the eutectics model simulation exhibits an earlier thermal challenge to the lower head by a greater mass of higher temperature debris. Figure 27 shows the temperature of the inner nodes of the lower head. Heat transfer to the lower head begins much later in the interactive materials model, which also exhibits later core plate failure and core slump to the lower plenum. In the interactive materials model simulation, lower head heatup is sustained across all inner lower head nodes from 7 hours until vessel failure, which is observed at a peak temperature of 1406.8 K. Conversely, a decrease in the temperature of the first radial segment is observed prior to vessel failure in the eutectics model simulation and the lower head is observed to fail at a higher peak temperature of 1507.7 K. The lower head failure models employed are the same for each simulation.

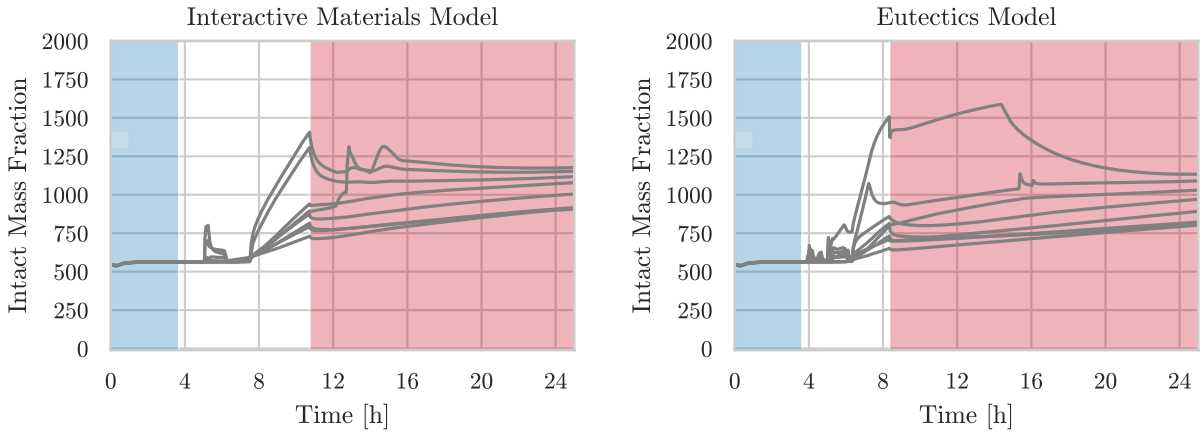

Figure 27. Comparison of lower head inner wall temperatures.

The masses of constituent materials ejected from the RPV are shown in Figure 28. Both models exhibit massive debris ejection upon lower head failure. Debris ejection events that are observed after lower head failure, in both simulations, occur after failure of remaining intact core structures (discussed in section 3.4). The interactive materials model simulation exhibits more debris formation, particularly in rings 3 and 4, after lower head failure than the eutectics model simulation. Consequently, the interactive materials model simulation also exhibits a prolonged period of debris ejection because the debris formed in the core must migrate to the RPV breach in the lower head. At 25 hours, the interactive materials model, which exhibits less debris formation, also exhibits less total ejected mass than the eutectics model simulation, 78.4 Mg compared to 89.4 Mg. Both simulations exhibit UO_2 to make up more than 50% of the total mass ejected, 51.2 Mg and 52.6 Mg for the eutectics and interactive materials model, respectively. Oxidized stainless steel makes up the smallest constituent mass of ejected debris for both simulations, 2.2 Mg and 2.7 Mg for the eutectics and interactive materials model, respectively. The eutectics model, which exhibited less core material oxidation, exhibits greater masses of ejected metallic debris (Zr and stainless steel) than the interactive materials model. Ejected Zr masses are 12.6 Mg and 7.2 Mg, and ejected stainless steel masses are 12.9 Mg and 5.3 Mg for the eutectics model simulation and interactive materials model simulation, respectively. The interactive materials model exhibits a larger mass of ejected ZrO_2, 10.5 Mg compared to 10.2 Mg.

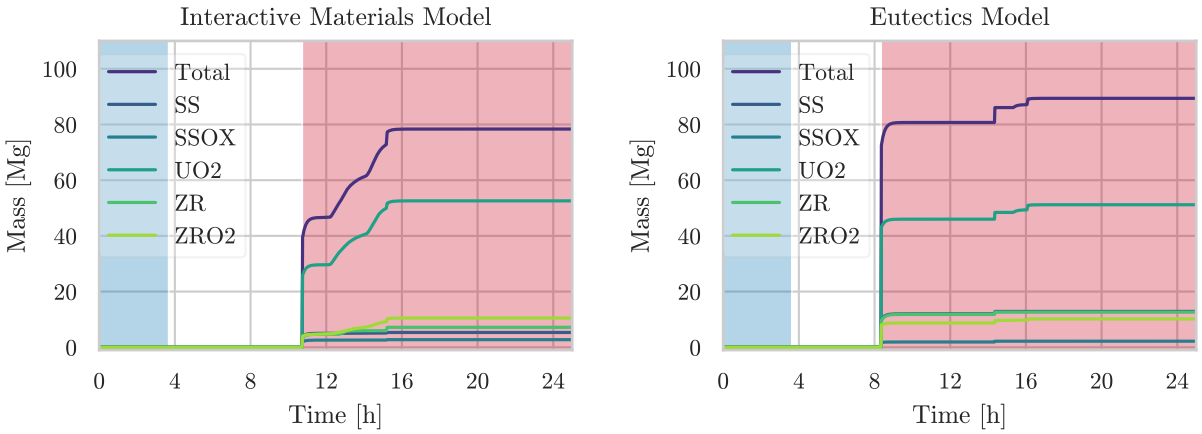

Figure 28. Comparison of ejected debris masses.

4. CONCLUSIONS

This benchmark comparison of the interactive materials model and eutectics model for a BWR under Fukushima Daiichi boundary conditions indicates that implementation of the eutectics model leads to simulation of an accelerated accident progression. Nearly all key accident signatures involving core degradation occurred earlier in the eutectics model simulation including initial SSC failures, first relocation of debris to the lower plenum, core plate failure, core slumping, lower plenum dryout, and RPV breach. A greater degree of core degradation is also exhibited by the eutectics model during the late in-vessel accident phase including larger peak molten debris mass; more complete destruction of the core; greater mass of total core debris, relocation to the lower plenum, and debris ejected. As a result of earlier destruction of core components, hydrogen generation and core materials oxidation ceases at an earlier time leading to lower masses of hydrogen and oxidized materials. Furthermore, lower core temperatures during the ex-vessel accident phase preclude a secondary, significant hydrogen generating transient that was observed in ring 5 of the interactive materials model simulation. In the eutectics model simulation, a greater mass of particulate debris relocates to the lower plenum earlier and subsequently reaches higher temperatures, presenting an earlier, greater thermal challenge to the lower head; accelerating both lower head heat-up and its ultimate failure. Finally, the user-defined liquefaction temperature of ZrO_2-interactive and UO_2-interactive is found to effectively limiting maximum temperatures that can be reached by core materials and components, and consequently the maximum ΔT possible in the core, for the interactive materials model. Such a limitation on core material and component temperatures is not observed in the eutectics model simulation. Material interactions have strong implications on the path and speed with which core degradation may occur in currently deployed LWR technologies. Material interactions, though different in detail, will continue to play a key role to the behavior of emergent accident tolerant fuel and next-generation reactors technologies under severe accident conditions.

ACKNOWLEDGEMENTS

We thank Jesse Phillips (SNL) for his time and effort reviewing this work.

Part of this work was conducted in coordination with the IAEA CRP I31033 on Advancing the State-of-Practice in Uncertainty and Sensitivity Methodologies for Severe Accident Analysis in Water Cooled Reactors.

This work was jointly supported by the U.S. DOE-NE IUP Fellowship Program and the United States Nuclear Regulatory Commission. The views expressed in the article do not necessarily represent the views of the U.S. Department of Energy or the United States Government.

Sandia National Laboratories is a multimission laboratory managed and operated by National Technology & Engineering Solutions of Sandia, LLC, a wholly owned subsidiary of Honeywell International Inc., for the U.S. Department of Energy's National Nuclear Security Administration under contract DE-NA0003525.

SAND2020-XXXXX X

REFERENCES

[1] P. Hoffman, "Current Knowledge on Core Degradation Phenomena, a Review," *Journal of Nuclear Materials,* vol. 270, pp. 194--211, 1999.

[2] L. L. Humphries, B. A. Beeny, C. Faucett, F. Gelbard, T. Haskin, D. L. Louie and J. Phillips, "MELCOR Computer Code Manuals Reference Manual, Vol. 2: Reference Manual," U.S. Nuclear Regulatory Commission, Washington, DC, 2019.

[3] L. L. Humphries, B. A. Beeny, F. Gelbard, D. L. Louie and J. Phillips, "MELCOR Computer Code Manuals Reference Manual, Vol. 1: Primer and Users' Guide," U.S. Nuclear Regulatory Commission, Washington, DC, 2019.

[4] B. R. Sehgal, Nuclear Safety in Light Water Reactors: Severe Accident Phenomenology, Oxford, UK: Academic Press, 2012.

[5] T. Haste and et al., "A Comparison of Core Degradation Phenomena in the CORA, QUENCH, Phébus SFD, and Phébus FP Experiments," *Nuclear Engineering and Design,* vol. 283, pp. 8-20, 2015.

[6] P. Hoffman and D. Kerwin-Peck, "UO_2/Zircaloy-4 Chemcal Interactions from 1000 to 1700˚C Under Isothermal and Transient Temperature Conditions," *Journal of Nuclear Materials,* vol. 124, pp. 80-105, 1984.

[7] K. T. Kim and D. R. Olander, "Dissolution of Uranium Dioxide by Molten Zircaloy, I. Diffusion-controlled Reaction," *Journal of Nuclear Materials,* vol. 154, pp. 85-101, 1988.

[8] K. T. Kim and D. R. Olander, "Dissolution of Uranium Dioxide by Molten Zircaloy, II. Convection-controlled Reaction," *Journal of Nuclear Materials,* vol. 154, pp. 102-155, 1988.

[9] P. J. Hayward and I. M. George, "Dissolution of ZrO_2 in Molten Zircaloy-4," *Journal of Nuclear Materials,* vol. 265, pp. 69-77, 1999.

[10] P. J. Hayward and I. M. George, "Dissolution of UO_2 in Molten Zircaloy-4, Part 1: Solubility from 2000 to 2000 ˚C," *Journal of Nuclear Materials,* vol. 208, pp. 35-42, 1994.

[11] M. S. Veshchunov and P. Hoffman, "Dissolution of Solid UO_2 by Molten Zircaloy," *Journal of Nuclear Materials,* vol. 209, pp. 27-40, 1994.

[12] P. Nikolopoulos, P. Hoffman and D. Kerwin-Peck, "Determination of the Interfacial Energy and Work of Adhesion in the UO_2/Zircaloy-4 Diffusion Couple," *Journal of Nuclear Materials,* vol. 124, pp. 106-113, 1984.

[13] C. R. Barrett, W. D. Nix and A. S. Tetelman, The Principles of Engineering Materials, Englewood Cliffs, New Jersey: Prentice-Hall, Inc., 1973.

[14] P. Hofmann, S. Hagen, G. Schanz and A. Skokan, "Chemical Interactions of Reactor Core Materials Up to Very High Temperatures," Kernforschungszentrum Karlsruhe, Karlstein, Germany, 1989.

[15] C. Gueneau, S. Gosse, A. Quaini, N. Dupin, B. Sundman, M. Kurata, T. Besmann, P. Turchi, J. Dumas, E. Corcoran, M. Piro, T. Ogata, R. Hania, B. Lee, R. Kennedy and S. Massara, "FUELBASE,TAF-ID Databases and OC Software: Advanced Computational Tools to Perform Thermodynamic Calculations on Nuclear Fuel Materials," in *The 7th European Review Meeting on Severe Accident Research*, Marseille, France, 2015.

[16] P. Mattie, R. Gauntt, K. Ross, N. Bixler, D. Osborn, C. Sallaberry, J. Jones and T. Ghosh, "State-of-the-Art Reactor Consequence Analysis Project: Uncertainty Analysis of the Unmitigated Long-Term Station Blackout of the Peach Bottom Atomic Power Station," U.S. Nuclear Regulatory Commission, Washington, D.C., 2016.

[17] Sandia National Laboratories, "State-of-the-Art Reactor Consequence Analysis Project, Vol. 1: Peach Bottom Integrated Analysis," U.S. Nuclear Regulatory Commission, Washington, D.C., 2013.

[18] OECD Nuclear Energy Agency, "Benchmark Study of the Accident at the Fukushima Daiichi Nuclear Power Plant - (BSAF Project) -- Phase I Summary Report," OECD/NEA/CSNI, 2016.

[19] L. I. Albright, N. Andrews, L. L. Humphries, R. O. Gauntt and T. Jevremovic, "Uncertainty Analysis of Corium Relocation to the Lower Plenum Using Results from The OECD/NEA BSAF Phase II Project," in *NURETH-18*, Portland,OR, August, 2019.

[20] N. Andrews, C. Faucett, T. Haskin, N. Bixler, D. Clayton and R. Gauntt, *Sandia National Laboratories' Contribution to the OECD/NEA BSAF Phase II Project,* United States, 2019.

[21] L. I. Albright, N. Andrews, L. L. Humphries, D. L. Luxat and T. Jevremovic, "Material Interactions in Severe Accidents - Benchmarking the MELCOR V2.2 Eutectics Model for a BWR-3 Mark-I Station Blackout: Part II - Uncertainty Analysis," *Submitted.*

[22] J. N. Cardoni, "Radionuclide Inventory and Decay Heat Quantification Methodology for Severe Accident Simulations," Sandia National Laboratories, Albuquerque, New Mexico, 2014.

[23] EPRI, "Modular Accident Analysis Program (MAAP) – MELCOR Crosswalk: Phase 1 Study," EPRI, Palo Alto, California, 2014.